

**Antenas 5G para acceso fijo a Internet con mejora de capacidad - 5G AFIANCE  
THD 2019**



**5GAFIANCE – Antenas 5G para acceso fijo a  
Internet con mejora de capacidad**

***5G antennas for fixed Internet access with  
capacity enhancement***

**E10 – Integración de subsistemas de antena y  
pruebas**

***D10 – Antenna subsystem integration and  
testing***

Original Delivery Date:	March 29 2021
Actual Delivery Date:	March 29 <sup>th</sup> 2022
Editor:	Nokia
Work Package:	PT4
Version:	1.0
Number of Pages:	67

Dissemination Level		
PU	Public	
PP	Restricted to other participants of the program	
RE	Restricted to a specific group defined by the consortium	
CO	Confidential, only for the members of the consortium	X

## E10 – Integración de subsistemas de antena y pruebas

<b>VERSION DETAILS</b>	
Version:	1
Date:	March 29 <sup>th</sup> 2021
State:	Draft Version

<b>PARTICIPANTS</b>	
<b>Participant</b>	<b>Name</b>
UC3M	Jose Manuel Poyanco Acevedo
UC3M	Eva Rajo Iglesias
UC3M	Matilde Sánchez Fernández

<b>DOCUMENT HISTORY</b>			
<b>Version</b>	<b>Date</b>	<b>Responsible</b>	<b>Description</b>
1	March 29 <sup>th</sup> 2022	UC3M	

<b>DELIVERABLE REVIEWS</b>			
<b>Version</b>	<b>Date</b>	<b>Reviewed by</b>	<b>Conclusion*</b>

p.e. Accepted, Develop, Modify, Re-edit, Update

# Contents

Figures.....	4
Executive Summary .....	9
Resumen Ejecutivo.....	9
1     Introduction .....	10
2     Antenna measurements. ....	11
2.1     Conformal patches .....	11
2.1.1     Dual slot patch antenna covering b40 (2.3 – 2.4 GHz) and n77 (3.3 – 4.2 GHz) frequency bands.	12
2.1.2     Single linear slot conformal patch antenna covering b40 and b42 frequency band. ....	20
2.1.3     Single “U” shape slot conformal patch antenna covering b40 and b42 frequency bands...	23
2.2     Mm-wave phased array patch antenna as reflector feed .....	27
2.2.1     Phased array patch antenna. ....	27
3     Channel characterization measurements for beamforming strategies. ....	44
3.1     Indoor-indoor channel measurement .....	44
3.2     Indoor-outdoor measurements .....	49
3.2.1     First scenario.....	49
3.2.2     Second scenario .....	55
4     Subsystem integration and testing .....	60
4.1     Mm-wave channel measurement .....	60
4.2     Sub-6 GHz channel measurement.....	61
5     Conclusions.....	64
6     Annex .....	65
7     References .....	67

# Figures

<b>Fig. 1 3D model of dual slot patch conformal patch antenna design. ....</b>	<b>12</b>
<b>Fig. 2 Simulated reflection coefficient of dual slot conformal patch antenna. ....</b>	<b>12</b>
<b>Fig. 3 Simulated transmission coefficient of dual slot conformal patch antenna. ....</b>	<b>13</b>
<b>Fig. 4 Simulated maximum gain versus frequency of dual slot patch conformal antenna. ....</b>	<b>13</b>
<b>Fig. 5 Measured copper prototype on an anechoic chamber of dual slot conformal patch antenna. ....</b>	<b>13</b>
<b>Fig. 6 Simulated and measured reflection coefficient of dual slot conformal patch antenna copper prototype – Port 1. ....</b>	<b>14</b>
<b>Fig. 7 Simulated and measured reflection coefficient of dual slot conformal patch antenna copper prototype – Port 2. ....</b>	<b>14</b>
<b>Fig. 8 Simulated and measured transmission coefficient between port two ports of dual slot conformal patch antenna copper prototype. ....</b>	<b>15</b>
<b>Fig. 9 Measured maximum gain versus frequency of dual slot conformal patch antenna copper prototype, in both planes at b40 frequency band. ....</b>	<b>15</b>
<b>Fig. 10 Measured maximum gain versus frequency of dual slot conformal patch antenna copper prototype, in both planes at b42 frequency band. ....</b>	<b>16</b>
<b>Fig. 11 Silver paint prototype of dual slot conformal patch antenna. ....</b>	<b>17</b>
<b>Fig. 12 Measured reflection coefficient of both ports and transmission coefficient between ports of dual slot conformal patch antenna silver paint prototype. ....</b>	<b>17</b>
<b>Fig. 13 Measured maximum gain versus frequency of port 1 of dual slot conformal patch antenna silver paint prototype. ....</b>	<b>18</b>
<b>Fig. 14 Measured maximum gain versus frequency of port 2 of dual slot conformal patch antenna silver paint prototype. ....</b>	<b>18</b>
<b>Fig. 15 Planar version milling prototype of dual slot conformal patch antenna. ....</b>	<b>18</b>
<b>Fig. 16 Measured maximum gain versus frequency of planar version milling prototype of dual slot conformal patch antenna. ....</b>	<b>19</b>
<b>Fig. 17 Single linear slot conformal patch antenna model. ....</b>	<b>20</b>
<b>Fig. 18 Simulated reflection coefficient of both ports and transmission coefficient between ports of single linear slot conformal patch antenna. ....</b>	<b>20</b>
<b>Fig. 19 Simulated maximum gain versus frequency of two ports of single linear slot conformal patch antenna. ....</b>	<b>21</b>
<b>Fig. 20 Silver paint prototype of single linear slot conformal patch antenna. ....</b>	<b>21</b>

<b>Fig. 21 Measured reflection coefficient of two ports and transmission coefficient between ports of silver paint prototype of single slot conformal patch antenna.....</b>	<b>21</b>
<b>Fig. 22 Measured maximum gain versus frequency of silver paint prototype of single slot conformal patch antenna. ....</b>	<b>22</b>
<b>Fig. 23 Model of U shape slot conformal patch antenna. ....</b>	<b>23</b>
<b>Fig. 24 Simulated reflection coefficient of two port and transmission coefficient between ports of U shape slot conformal patch antenna. ..</b>	<b>23</b>
<b>Fig. 25 Simulated maximum gain versus frequency of two ports of U shape slot conformal patch antenna. ....</b>	<b>24</b>
<b>Fig. 26 Prototype of U shape slot conformal patch antenna. ....</b>	<b>24</b>
<b>Fig. 27 Measured reflection coefficient of two ports and transmission coefficient between ports of U shape slot conformal patch antenna. ..</b>	<b>24</b>
<b>Fig. 28 Measured maximum gain versus frequency of two ports of U shape slot conformal patch antenna. ....</b>	<b>25</b>
<b>Fig. 29 Normalized measured radiation pattern of port one at central frequency of b40 band of U shape slot conformal patch antenna. ....</b>	<b>25</b>
<b>Fig. 30 Normalized measured radiation pattern of port two at central frequency of b40 band of U shape slot conformal patch antenna. ....</b>	<b>26</b>
<b>Fig. 31 Normalized measured radiation pattern of port one at central frequency of b42 band of U shape slot conformal patch antenna. ....</b>	<b>26</b>
<b>Fig. 32 Normalized measured radiation pattern of port two at central frequency of b42 band of U shape slot conformal patch antenna. ....</b>	<b>27</b>
<b>Fig. 33 Simulated radiation pattern of the phased array patch antennas..</b>	<b>27</b>
<b>Fig. 34 Unassembled prototypes of phased array patch antennas. ....</b>	<b>28</b>
<b>Fig. 35 Assembled prototype of phased array patch antenna. ....</b>	<b>28</b>
<b>Fig. 36 Photo of measuring process of phased array patch antenna - 30° phase shift version.....</b>	<b>28</b>
<b>Fig. 37 Measured reflection coefficient of 30° phase shift of phased array patch antenna.....</b>	<b>29</b>
<b>Fig. 38 Measured radiation pattern of 30° phase shift patch array at 26 GHz. ....</b>	<b>29</b>
<b>Fig. 39 Measured radiation pattern of 30° phase shift patch array at 28 GHz. ....</b>	<b>30</b>
<b>Fig. 40 Measured radiation pattern of 30° phase shift patch array at 30 GHz. ....</b>	<b>30</b>
<b>Fig. 41 Measured gain versus frequency of 30° phase shift phased array patch antenna.....</b>	<b>31</b>
<b>Fig. 42 Normalized measured and simulated radiation pattern of 30° phase shift phased array patch antenna at 28 GHz.....</b>	<b>31</b>
<b>Fig. 43 Measured radiation pattern of 60° phase shift patch array at 26 GHz. ....</b>	<b>32</b>
<b>Fig. 44 Measured radiation pattern of 60° phase shift patch array at 28 GHz. ....</b>	<b>32</b>

<b>Fig. 45 Measured radiation pattern of 60° phase shift patch array at 30 GHz.</b> .....	32
<b>Fig. 46 Normalized measured and simulated radiation pattern of 60° phase shift phased array patch antenna at 28 GHz.....</b>	33
<b>Fig. 47 Front view of U shape slot patch antennas conformal to the reflector fed by phased array patch antennas. ....</b>	33
<b>Fig. 48 Back view of U shape slot patch antennas conformal to the reflector fed by phased array patch antennas. ....</b>	34
<b>Fig. 49 Photo of measured prototype. Focus to phased array patch antenna. ....</b>	34
<b>Fig. 50 Photo of measured assembled prototype. ....</b>	34
<b>Fig. 51 Photo of measured assembled prototype. ....</b>	35
<b>Fig. 52 Mm-wave measured radiation pattern of assembled prototype at 26 GHz. Feed of mm-wave patch array with phase shift of 30°.....</b>	35
<b>Fig. 53 Mm-wave measured radiation pattern of assembled prototype at 28 GHz. Feed of mm-wave patch array with phase shift of 30°.....</b>	36
<b>Fig. 54 Mm-wave measured radiation pattern of assembled prototype at 30 GHz. Feed of mm-wave patch array with phase shift of 30°.....</b>	36
<b>Fig. 55 Mm-wave measured versus simulated radiation pattern of assembled prototype at 28 GHz. Feed of mm-wave patch array with phase shift of 30°. ....</b>	36
<b>Fig. 56 Mm-wave normalized measured versus simulated radiation pattern of assembled prototype at 28 GHz. Feed of mm-wave patch array with phase shift of 30°. ....</b>	37
<b>Fig. 57 Mm-wave measured radiation pattern of assembled prototype at 26 GHz. Feed of mm-wave patch array with phase shift of 60°.....</b>	37
<b>Fig. 58 Mm-wave measured radiation pattern of assembled prototype at 28 GHz. Feed of mm-wave patch array with phase shift of 60°.....</b>	38
<b>Fig. 59 Mm-wave measured radiation pattern of assembled prototype at 30 GHz. Feed of mm-wave patch array with phase shift of 60°.....</b>	38
<b>Fig. 60 Mm-wave measured versus simulated radiation pattern of assembled prototype at 28 GHz. Feed of mm-wave patch array with phase shift of 60°. ....</b>	38
<b>Fig. 61 Mm-wave normalized measured versus simulated radiation pattern of assembled prototype at 28 GHz. Feed of mm-wave patch array with phase shift of 60°. ....</b>	39
<b>Fig. 62 Measured gain versus frequency of mm-wave phased array patch antenna with 60° of phase shift, reflector antenna fed phased array and reflector antenna with conformal patches fed by this phased array patch antenna.....</b>	39
<b>Fig. 63 Measured prototypes of reflector antenna fed by phased array patch antennas with 60° of phase shift without conformal patches (blue borders) and with conformal patches (red borders).....</b>	40

<b>Fig. 64 Measured E-Plane radiation patterns of reflector with conformal patches prototype between 26 and 30 GHz. Phased array with 60° of phase shift.....</b>	<b>40</b>
<b>Fig. 65 Measured H-Plane radiation patterns of reflector with conformal patches prototype between 26 and 30 GHz. Phased array with 60° of phase shift.....</b>	<b>41</b>
<b>Fig. 66 Measured E-Plane radiation patterns of reflector without conformal patches prototype between 26 and 30 GHz. Phased array with 60° of phase shift.....</b>	<b>41</b>
<b>Fig. 67 Measured H-Plane radiation patterns of reflector without conformal patches prototype between 26 and 30 GHz. Phased array with 60° of phase shift.....</b>	<b>42</b>
<b>Fig. 68 Measured and simulated gain versus frequency between 26 and 30 GHz of phased array patch antenna with 60° of phase shift.....</b>	<b>42</b>
<b>Fig. 69 Measured and simulated gain versus frequency between 26 and 30 GHz of reflector antenna with conformal patches fed by phased array patch antenna with 60° of phase shift. ....</b>	<b>42</b>
<b>Fig. 70 First indoor-outdoor measurement scenario plan.....</b>	<b>44</b>
<b>Fig. 71 Indoor-indoor channel measurement results between right transmitter antenna and receiver antenna at six different positions. Azimuthal rotation. ....</b>	<b>45</b>
<b>Fig. 72 Indoor-indoor channel measurement between right transmitter antenna and receiver antenna at six different positions. Elevation rotation at highest measured power in azimuthal of each position. ....</b>	<b>46</b>
<b>Fig. 73 Indoor-indoor channel measurement results between left transmitter antenna and receiver antenna at six different positions. Azimuthal rotation. ....</b>	<b>47</b>
<b>Fig. 74 Indoor-indoor channel measurement between left transmitter antenna and receiver antenna at six different positions. Elevation rotation at highest measured power in azimuthal of each position. ....</b>	<b>47</b>
<b>Fig. 75 Indoor-outdoor channel measurement results between transmitter antenna and receiver antenna at ten different positions. Azimuthal rotation. ....</b>	<b>50</b>
<b>Fig. 76 Indoor-outdoor channel measurement between transmitter antenna and receiver antenna at ten different positions. Elevation rotation at highest measured power in azimuthal of each position. ....</b>	<b>50</b>
<b>Fig. 77 Indoor-outdoor channel measurement polar results between transmitter antenna and receiver antenna at ten different positions. Azimuthal rotation. Red line: physical angle between receiver and transmitter antenna. Black dotted line: direction of maximum power.</b>	<b>51</b>
<b>Fig. 78 Indoor-outdoor measurement scenario and setup photograph. ....</b>	<b>51</b>
<b>Fig. 79 Indoor-outdoor channel polar measurement between transmitter antenna and receiver antenna at ten different positions. Elevation rotation at highest measured power in azimuthal of each position. ....</b>	<b>52</b>

<b>Fig. 80 Angular and height difference between transmitter and receiver antennas diagram. Top: realistic case. Bot: implemented case.</b>	.....	52
<b>Fig. 81 Indoor-outdoor channel measurement polar results between transmitter antenna and receiver antenna at five different positions with different height. Azimuthal rotation. Red line: physical angle between receiver and transmitter antenna. Black dotted line: direction of maximum power. Pink dotted line: direction of maximum global power of each position.</b>	.....	53
<b>Fig. 82 Indoor-outdoor channel polar measurement between transmitter antenna and receiver antenna at five different positions. Elevation rotation at highest measured global power of each position. Red circle: maximum global power of each position.</b>	.....	54
<b>Fig. 83 Second indoor-outdoor measurement scenario plan.</b>	.....	55
<b>Fig. 84 Second scenario of indoor-outdoor channel measurement polar results between transmitter antenna and receiver antenna at six different positions with different height. Azimuthal rotation. Red line: physical angle between receiver and transmitter antenna. Black dotted line.</b>	.....	56
<b>Fig. 85 Second scenario indoor-outdoor channel polar measurement between transmitter antenna and receiver antenna at six different positions. Elevation rotation at highest measured global power of each position. Red circle: maximum global power of each position.</b>	.....	56
<b>Fig. 86 Transmitting antenna positioning room for indoor-indoor measurements. Photo taken from the green arrow number 1 shown in Fig. 3.</b>	.....	57
<b>Fig. 87 Transmitting antenna positioning room for indoor-indoor measurements. Photo taken from the green arrow number 2 shown in Fig. 3.</b>	.....	58
<b>Fig. 88 Receiving antenna positioning room for indoor-indoor and indoor-outdoor measurements. Photo taken from the green arrow number 3 shown in Fig. 3.</b>	.....	58
<b>Fig. 89 Receiving antenna positioning room for indoor-indoor and indoor-outdoor measurements with view to the outdoor area where the transmitting antenna of these measurements will be positioned. Photo taken from the green arrow number 4 shown in Fig. 6.</b>	.....	58
<b>Fig. 90 Receiving antenna positioning room for indoor-indoor and indoor-outdoor measurements with view to the outdoor area where the transmitting antenna of these measurements will be positioned. Photo taken from the green arrow number 5 shown in Fig. 6.</b>	.....	59

# Executive Summary

This document details a novel design of antennas that include a new reflector and includes the results of the experiments that have been carried out for the designed antennas and the beamforming strategy. There is a first part where the multi-band antennas have been tested with different feed antennas to emulate the scanning in the millimeter wave band. Afterwards, a measurement campaign of channel measurement at the 28 GHz band was performed with an outdoor-indoor scenario for different locations with horn antennas at the corresponding frequency. Finally, in the final set of measurements, the designed antenna in the first part is used for the same type of measurements including as well the sub-6 bands.

# Resumen Ejecutivo

Este documento detalla un nuevo diseño de antenas que incluye nueva geometría del reflector e incluye también los resultados de los experimentos y medidas que se han llevado a cabo para validar las antenas y la estrategia de conformado de haz. La primera parte incluye el diseño y medidas de las antenas multi-banda donde se han probado distintos alimentadores para modelar el barrido en la banda de milimétricas. En segundo lugar, se ha llevado a cabo una campaña de medida de canal a 28GHz para caracterizar entornos en exteriores-interiores con antenas de bocina a la frecuencia de medida. Esta misma campaña se llevará a cabo con las antenas diseñadas incluyendo la caracterización en la banda sub-6.

# 1 Introduction

This project deals with design of antennas for fixed wireless access (FWA) in the bands where most of the designs have mobility requirements as one of the baseline criteria designs. Multiband operation is key to provide the desired service where different 5G bands maybe used to provide FWA.

This deliverable deals with the design of dual-band antennas following a novel structure where a reflector with different feeding structures works in the millimeter band and allows for different scanning scenarios. Also, embed in the reflector, we provide a seamless integration of sub-6 antennas, to provide the multiband aforementioned capability.

Channel propagation characterization is key, particularly in mmWave scenarios, where beamforming is the sole transmission strategy suitable. Propagation in mmWave follows a non diffuse mechanism, with very few propagation paths. For the beamforming strategy is key then to know the most frequent angle of arrivals, so that with the corresponding pointing mechanisms described in [2] we optimize the link budget.

This deliverable deals then with both topics, first the design of the dual-band antennas following a previous reflector structure of interest for Nokia and also the propagation characterization of the channel at 28GHz, both using commercial horn antennas and the antennas designed.

The experimental results are very critical and will be detailed in the following. First, the different antenna prototypes that were designed will be characterized. Mainly, it is important to check the realized gain in the different bands (and the matching that is related to it) and also the isolation between the two antennas used for diversity. The radiation patterns are a relevant as well to check that the antennas focalize the radiation as desired. For the proposed innovative design that combines conformal sub-6 patches with a reflector fed by a phased array of patches (at millimeter frequencies), it is critical to show that the presence of the patches do not destroy the performance of the reflector antenna in the millimeter band.

On the other hand, the channel measurements for different positions, angles, scenarios are an essential tool for this project as the conclusions derived from them, will be used in the strategy of beamforming that will be implemented in the system. This characterization will be made by using standard antennas. Finally, the last part of the activities related with the integration consists of using the designed antenna for the channel measurements.

## 2 Antenna measurements.

According to [1], different conformal patches to the surface of an existing reflector have been designed. Finally, this antenna will operate in millimeter frequency bands and in two sub-6 bands. The high frequency range will be covered by the reflector, which is fed by a phased array patch antenna at 28 GHz, and the sub-6 GHz bands by the reflector conformal patches. Specifically, these low frequency bands are b40 and b42, which are covered thanks to different slots designed on the patch antennas.

In the following, the different measurements planned in [2] and their results are shown. In addition, the measured prototypes are specified.

### 2.1 Conformal patches

In this project, three different models of patch antennas conformal to the reflector are designed, prototyped and measured. These conformal patch antennas have two main parts: the first one is the radiant element made of metal which have different shapes and different slots to increase its bandwidth. These metallic parts will be manufactured using self-adhesive copper sheets and silver paint.

The second conformal patch antenna main part is the substrate, which has critical parameters for the correct operation as the height and permittivity value. The height is set in lambda over 2 at the millimeter wave frequency (28 GHz), to ensure that the reflected wave on the reflector and on the patch are in phase. These substrates will be manufactured using 3D-printing with PLA material. To obtain the exact permittivity value of the design, the infill percentage will be varied to obtain values lower than the nominal. This is a well-known 3D-printers variable, which prints the model not completely solid in order to, in general, save material, but in this case this parameter is used to make a PLA-air mixture and obtain a lower permittivity value.

This PLA was initially characterized, obtaining a nominal permittivity value of 2.45. All the substrate of the conformal patch array were designed with a permittivity value of 1.65, which can be obtained with a 49% of infill.

After the first round of measurement of each of the designed conformal patch antennas, it was concluded that the initial curve of infill percentage versus permittivity value needed an adjustment. This was concluded after obtaining all antenna resonances at a lower frequency, which meant that the permittivity value of the substrates was higher than necessary. This phenomenon occurred in all models, in the same proportion, which pointed to the above-mentioned conclusion.

The following are three designs of patch antennas conforming to the reflector, previously explained in [2]. It is important to note that in all designs, two conformal

patch antennas will be placed in the reflector surface, rotated ninety degrees with respect to each other, to obtain polarization diversity.

### **2.1.1 Dual slot patch antenna covering b40 (2.3 – 2.4 GHz) and n77 (3.3 – 4.2 GHz) frequency bands.**

First, we design a dual slot conformal patch antenna that covers b40 and n77 frequency band. This multiband and broadband behavior was achieved designing two different slots on the radiant structure. The designed model is shown in Fig. 1.

This model was placed on the reflector antenna and simulated, obtaining the reflection coefficient lower than -7 dB for all the frequencies inside the bands. Fig. 2 shows these results for both ports. Also, the coupling between ports was studied, in order to ensure a good isolation (below -20 dB) between them. Fig. 3 shows this result. Finally, the gain versus frequency is shown in Fig. 4. From this figure it can be seen that both patches have gain between 6 and 9 dB for all b40 and n77 frequency bands.

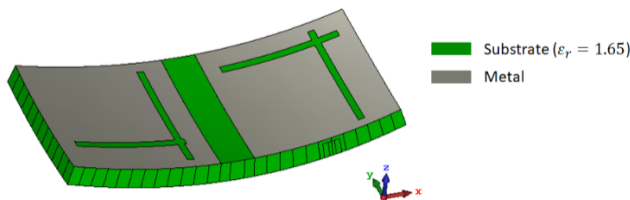


*Fig. 1 3D model of dual slot patch conformal patch antenna design.*

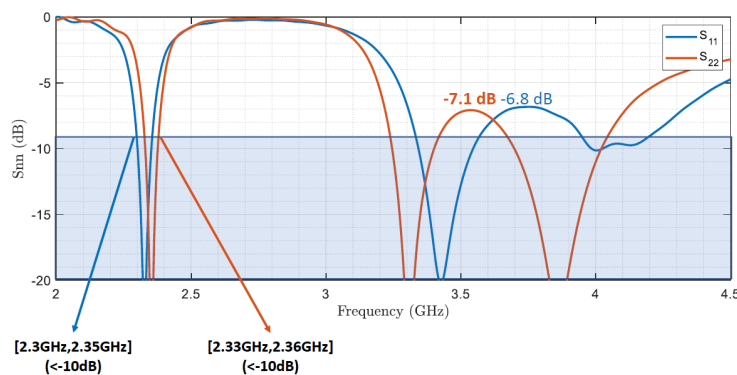


*Fig. 2 Simulated reflection coefficient of dual slot conformal patch antenna.*

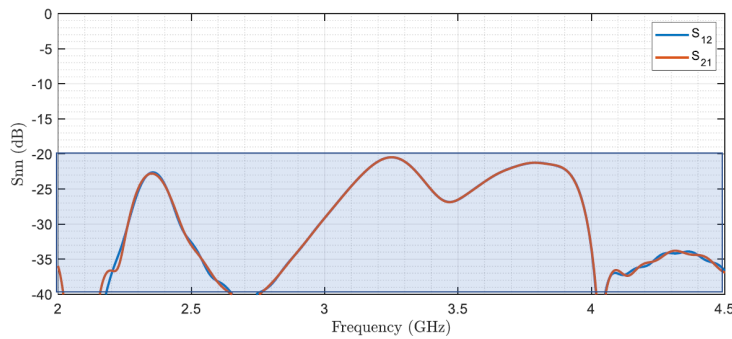


Fig. 3 Simulated transmission coefficient of dual slot conformal patch antenna.

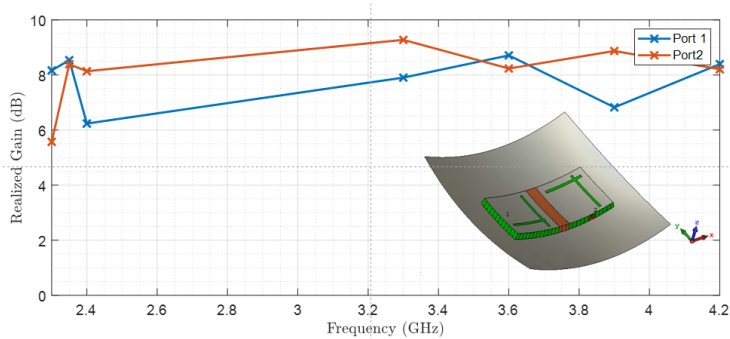


Fig. 4 Simulated maximum gain versus frequency of dual slot patch conformal antenna.

After ensuring that this model works through simulation, the first prototype was made, shown in Fig. 5. The radiant element of this prototype was made using copper self-adhesive sheets, cutting the slots as needed.

The reflection coefficient of each port and the coupling between them for this prototype were measured using a Vector Network Analyzer (VNA). The comparison between simulated and measured reflection coefficient is shown in Fig. 6 for port 1, and Fig. 7 for port 2. In addition, Fig. 8 shows the transmission coefficient between these two ports.

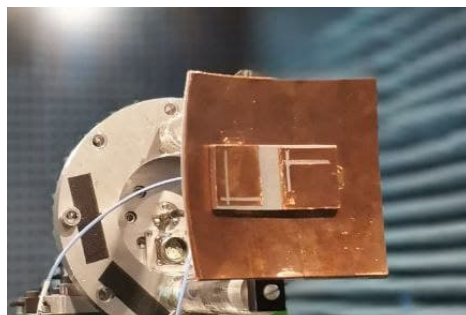
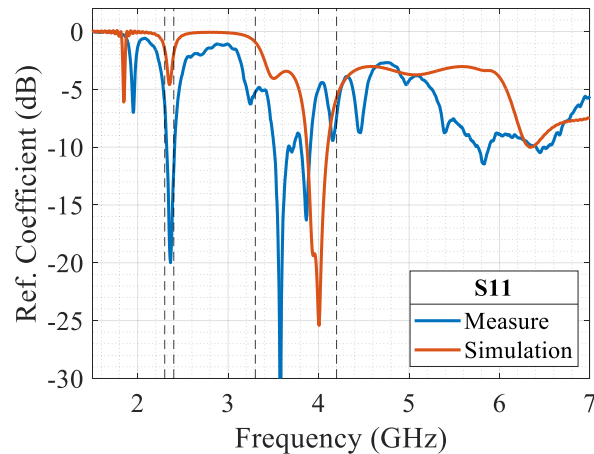


Fig. 5 Measured copper prototype on an anechoic chamber of dual slot conformal patch antenna.

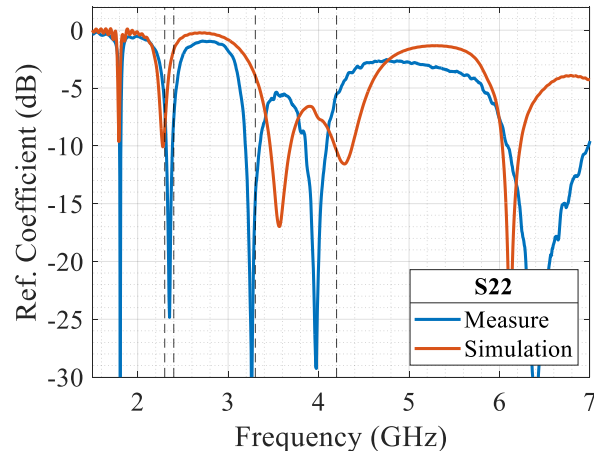
From these figures, it can be seen that both antennas are well matched and present good isolation.

Fig. 10 and Fig. 10 shows the measured gain versus frequency at b40 and n77 frequency band respectively. It can be seen that the antennas present a good behavior for b40 frequency band, but for n77 the gain decreases for the upper values of this band, showing a malfunction.

After several prototyping attempts using self-adhesive copper and obtaining similar results to those presented, it was decided to change the prototyping technique of the metallic part to use silver paint, which allows a greater degree of control over the dimensions, allowing to manufacture the slots with greater accuracy.



*Fig. 6 Simulated and measured reflection coefficient of dual slot conformal patch antenna copper prototype – Port 1.*



*Fig. 7 Simulated and measured reflection coefficient of dual slot conformal patch antenna copper prototype – Port 2.*

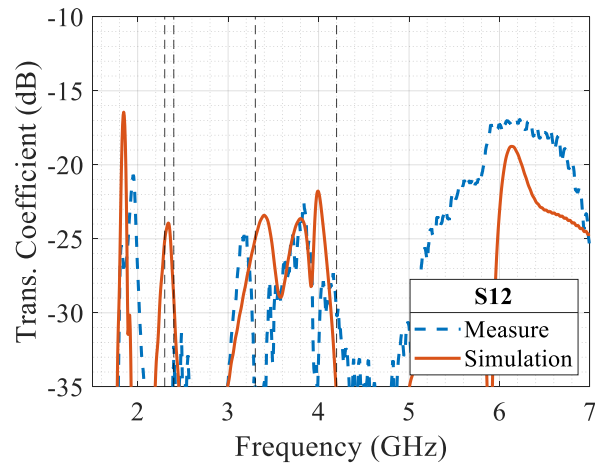


Fig. 8 Simulated and measured transmission coefficient between port two ports of dual slot conformal patch antenna copper prototype.

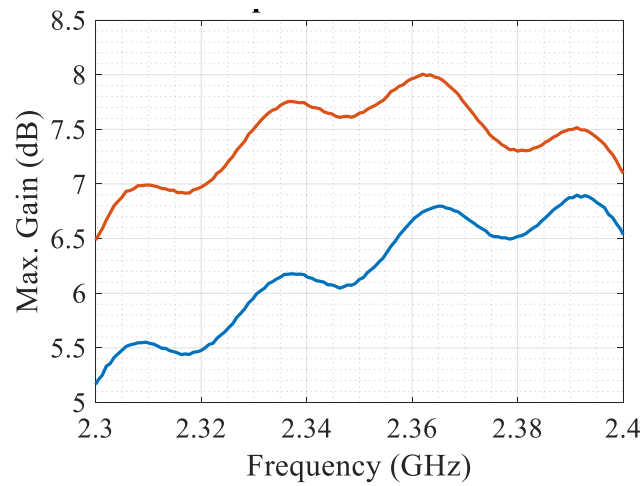


Fig. 9 Measured maximum gain versus frequency of dual slot conformal patch antenna copper prototype, in both planes at b40 frequency band.

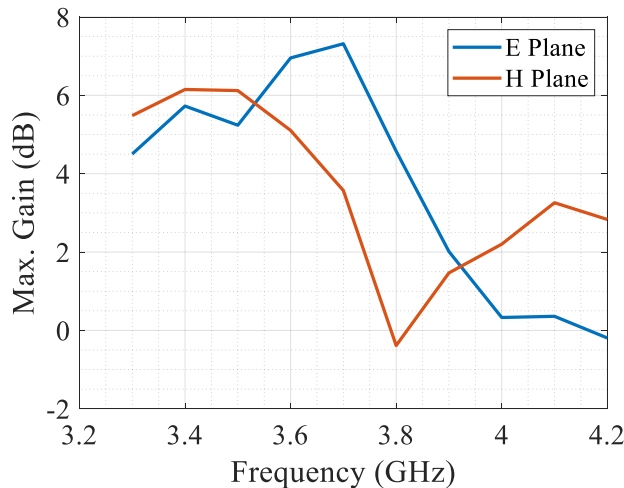


Fig. 10 Measured maximum gain versus frequency of dual slot conformal patch antenna copper prototype, in both planes at b42 frequency band.

The silver-painted prototype is shown in Fig. 11. From Fig. 12, which shows the reflection coefficient of each port and the coupling between them, it can be seen that the resonance frequencies are slightly shifted. Fig. 13 and Fig. 14 show the measured gain for the frequency range of interest. It can be seen that the gain values achieved are much lower than the results obtained by simulation, which is not related to the shift of the resonance frequencies.

To find out if the results obtained were related to a bad design or incorrect manufacturing, it was decided to make a flat version of this antenna with double slot, manufactured by a milling machine. Fig. 15 shows this prototype and Fig. 16 the gain achieved for the frequencies of interest. As it can be seen in the latter figure, the gain values achieved are good, and the patch resonates at the corresponding frequencies.

With these results it was confirmed that the antenna is well designed, but we are unable to manufacture it due to the high level of precision required for the slots. Also, since the slots are on a curved surface, it is not possible to manufacture it using the same method as for the flat version. Another difference comes from the feeding that in the case of the conformal version was made by capacitive coupling and in the flat version it was made directly with a SMA connector.

For the reasons explained here, it was decided to make another design, but this time covering the b40 and b42 bands.

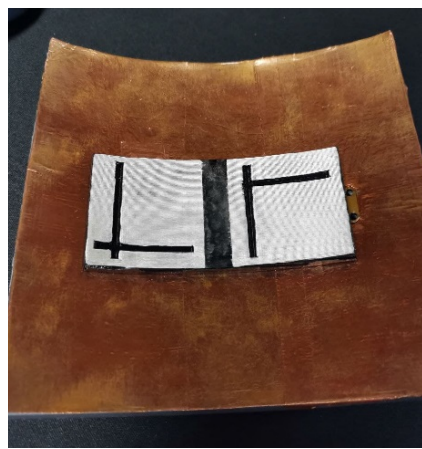


Fig. 11 Silver paint prototype of dual slot conformal patch antenna.

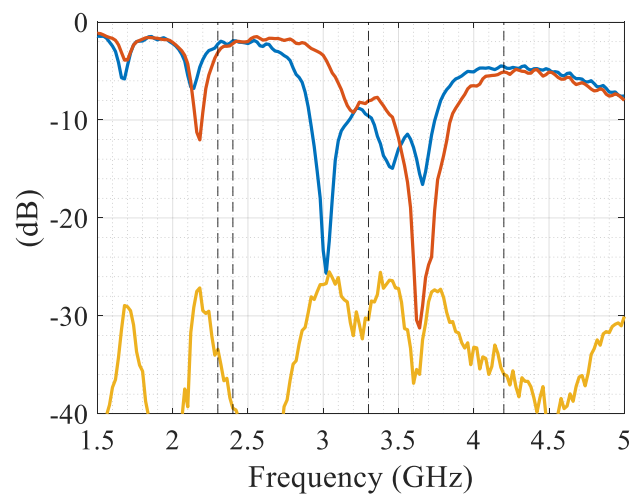


Fig. 12 Measured reflection coefficient of both ports and transmission coefficient between ports of dual slot conformal patch antenna silver paint prototype

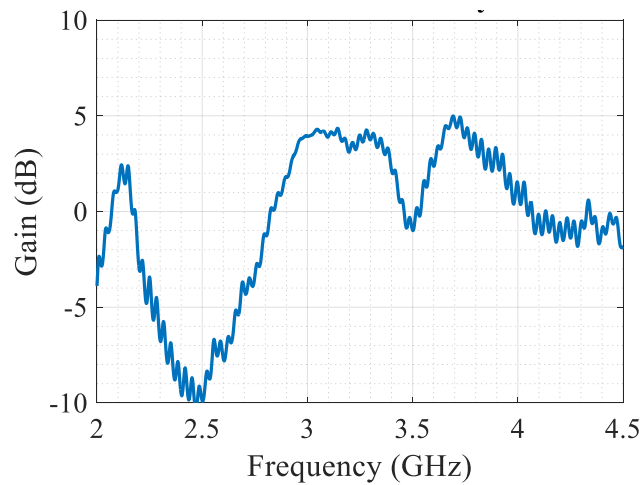


Fig. 13 Measured maximum gain versus frequency of port 1 of dual slot conformal patch antenna silver paint prototype.

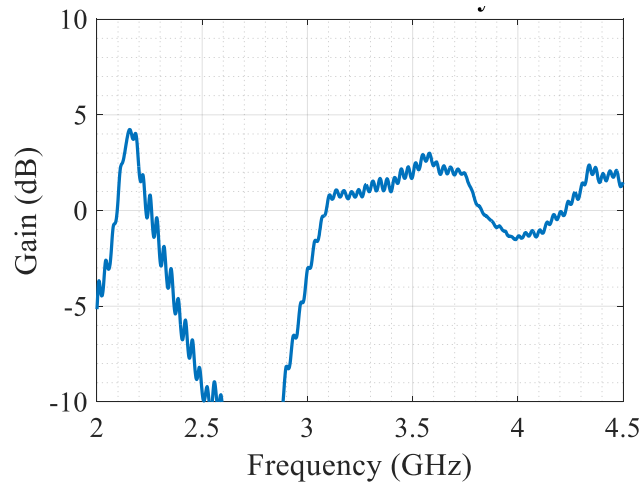
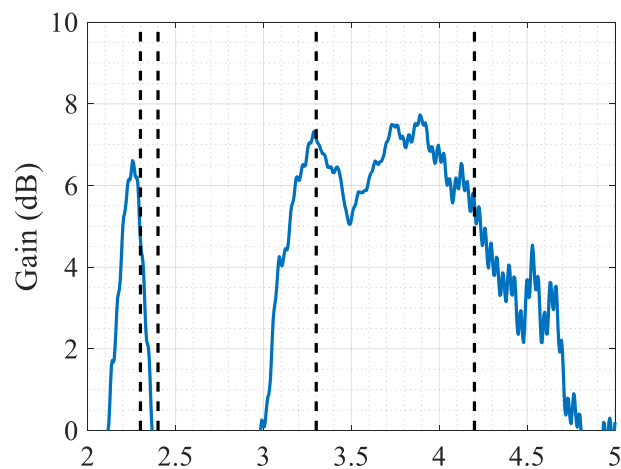


Fig. 14 Measured maximum gain versus frequency of port 2 of dual slot conformal patch antenna silver paint prototype.



Fig. 15 Planar version milling prototype of dual slot conformal patch antenna.



*Fig. 16 Measured maximum gain versus frequency of planar version milling prototype of dual slot conformal patch antenna.*

### 2.1.2 Single linear slot conformal patch antenna covering b40 and b42 frequency band.

The second designed model is shown in Fig. 17. This patch antenna has a single rectangular slot parallel to the feed plane. Two antennas were placed on the reflector surface and simulated. The reflection coefficients of port 1 and 2 and the transmission coefficient between them are shown in Fig. 18. Both antennas are well matched for b40 and b42 frequency bands, but present a higher transmission coefficient than the previous design for the lower band. Even so, this value is close to -15 dB, which is considered good.

Fig. 19 shown the maximum gain versus frequency for the studied bandwidth. Both antennas have gain values between 8 and 9 dB for the lower and higher frequency bands.

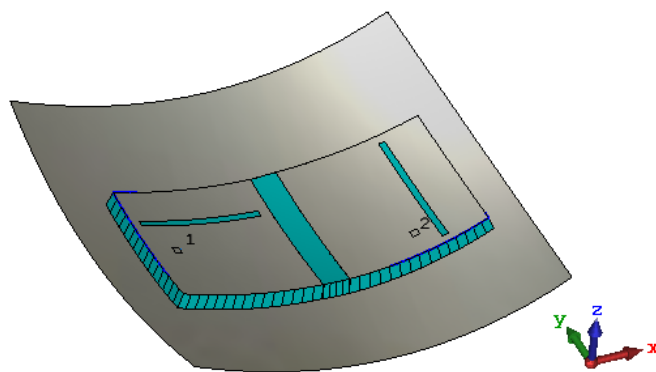


Fig. 17 Single linear slot conformal patch antenna model.

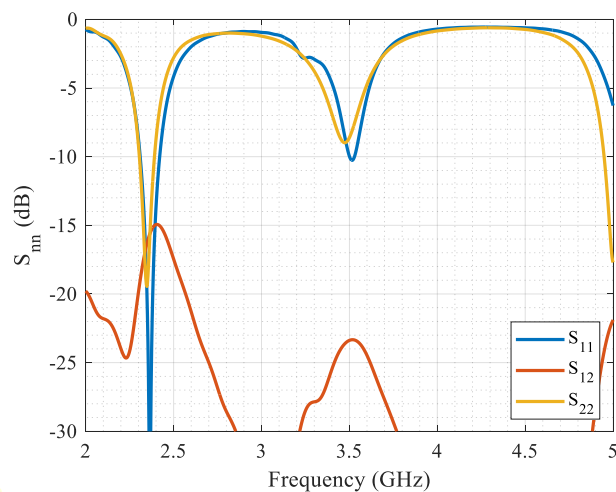


Fig. 18 Simulated reflection coefficient of both ports and transmission coefficient between ports of single linear slot conformal patch antenna.

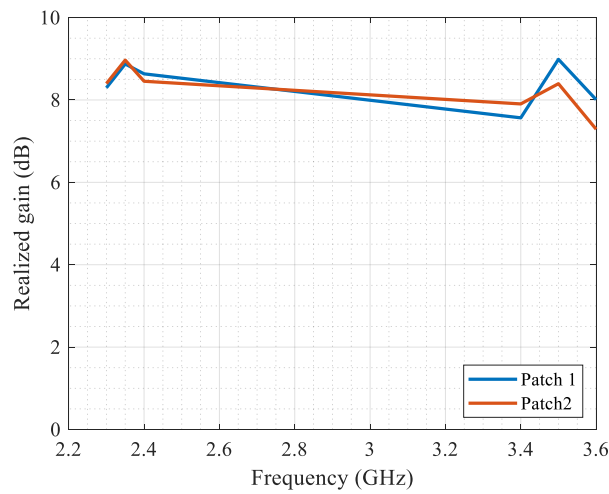


Fig. 19 Simulated maximum gain versus frequency of two ports of single linear slot conformal patch antenna.

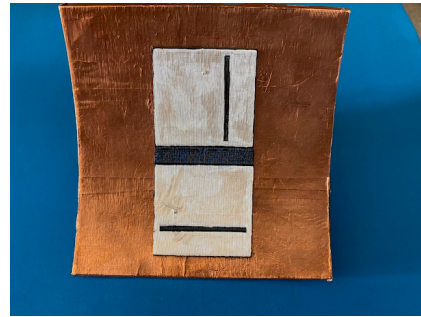


Fig. 20 Silver paint prototype of single linear slot conformal patch antenna.

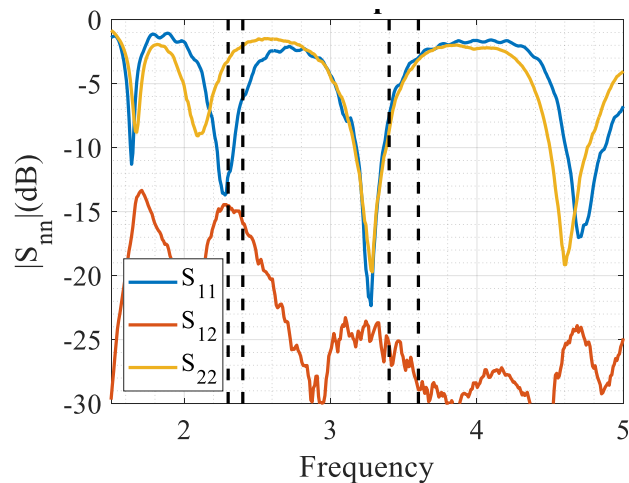


Fig. 21 Measured reflection coefficient of two ports and transmission coefficient between ports of silver paint prototype of single slot conformal patch antenna.

Once the simulation results show good performance in terms of matching, isolations between ports and gain, this single slot conformal patch antenna is considered as a good candidate for covering b40 and b42 frequency bands, proceeding to the manufacturing process.

Fig. 20 shown the manufactured prototype. It can be seen that the radiating element is made with silver paint. First, the reflection coefficient for each port and the coupling between them were measured and then, the gain versus frequency as shown in Fig. 21 and Fig. 22 respectively. From Fig. 21 it can be seen that the resonance frequencies were slightly shifter to lower frequency values and the transmission coefficient between ports were very close to the simulated value. From Fig. 22 it can be seen that the gain values are close to 6 dB for both ports for both frequency bands, but slightly shifted too. From this same figure, it can be seen that the curve of the same port has two different colors. For example, port one is blue for the low band and red for the high band. On the other hand, port two is colored purple for the low band and yellow for the high band. This occurred because for the same patch, the polarization of the wave in the low band is rotated ninety degrees with respect to the polarization in the high band. This is because the slot is in a plane parallel to the feed plane, and since the polarization of a slot in a patch is orthogonal to its length due to the excitation currents, we obtained a patch radiating with a polarization given by the feed plane for the low band, and the slot radiating with a polarization orthogonal to that of the patch for the high band.

This phenomenon adds a degree of difficulty, so it was decided to design another antenna covering both bands but with the same polarization in a single conformal patch antenna.

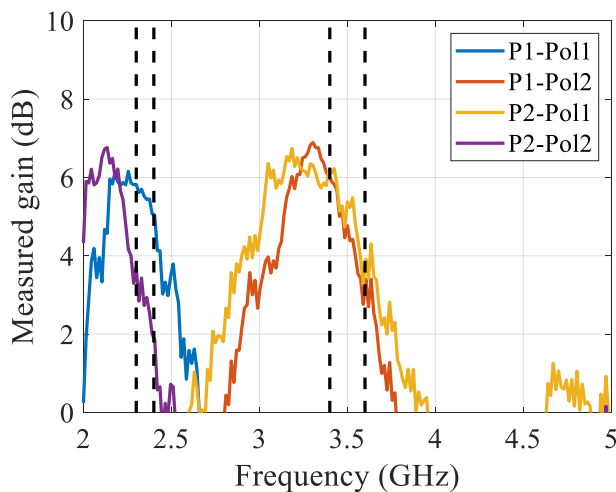


Fig. 22 Measured maximum gain versus frequency of silver paint prototype of single slot conformal patch antenna.

### **2.1.3 Single “U” shape slot conformal patch antenna covering b40 and b42 frequency bands.**

The third and last model is a single “U” shape slot conformal patch antenna, as shown in Fig. 23. This slot is placed around the feed, which is at the center of the patch. Fig. 24 shows the simulation results of reflection coefficient for each port and the transmission coefficient between them and Fig. 25 shows the maximum gain obtained for both patches at the frequency bands of interest.

This simulation results shows a good behavior of the antenna: both frequency bands of both conformal patch antennas present good matching, the isolation between the ports is lower than -20 dB and the obtained maximum gains are between 6 and 9 dB for both frequency bands.

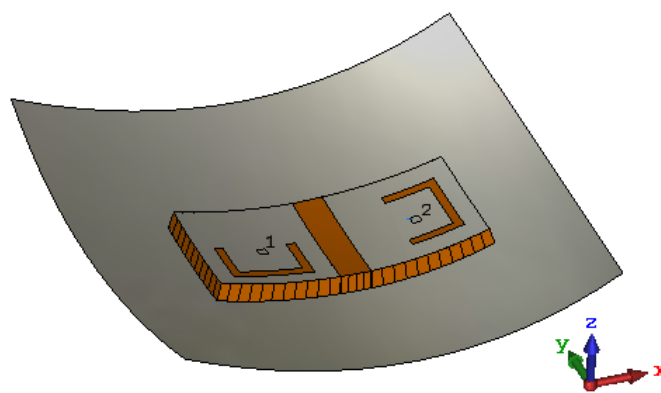


Fig. 23 Model of U shape slot conformal patch antenna.

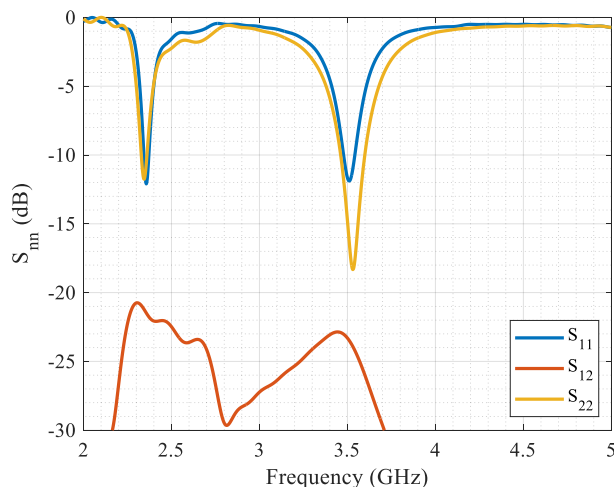


Fig. 24 Simulated reflection coefficient of two port and transmission coefficient between ports of U shape slot conformal patch antenna.

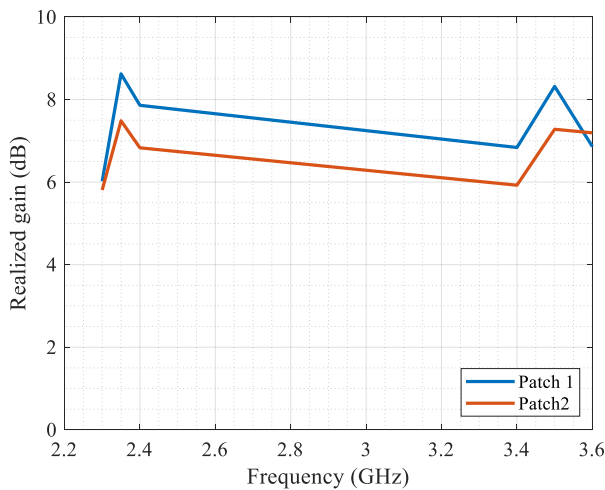


Fig. 25 Simulated maximum gain versus frequency of two ports of U shape slot conformal patch antenna.



Fig. 26 Prototype of U shape slot conformal patch antenna.

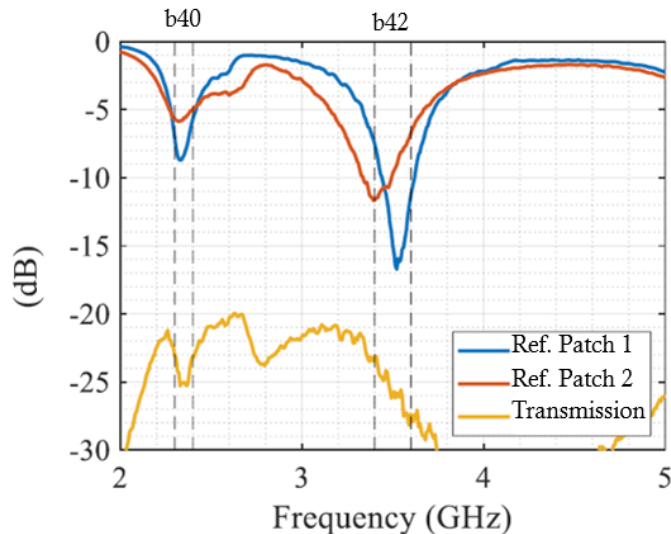


Fig. 27 Measured reflection coefficient of two ports and transmission coefficient between ports of U shape slot conformal patch antenna.

Once it was confirmed that the “U” shape slotted conformal patch antennas were well designed through simulation results, it was prototyped. Fig. 26 shown the

manufactured prototype. The metallic part of this design of conformal patch antenna was also silver-painted, to be able to paint the areas around the slots with precision. Fig. 27 shown the measured reflection coefficient for both ports and the transmission coefficient that shows that both ports are well isolated between them. Fig. 28 shows the measured gain values for the frequencies of interest, reaching values around 6 dB for both frequency bands. In addition, Fig. 29, Fig. 30, Fig. 31, and Fig. 32 show the measured far field radiation pattern for both ports, in both planes, for the central frequencies of both bands. It is important to say that the beam tilt is due to the curved shape that have each conformal patch antenna, pointing slightly off center.

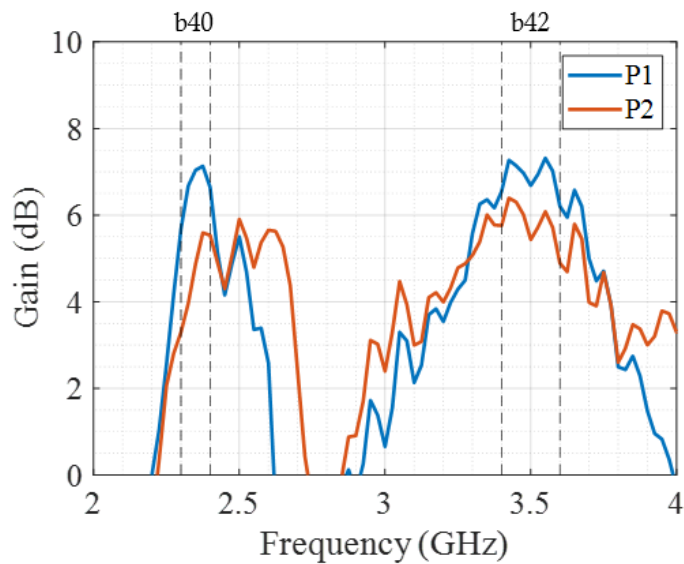


Fig. 28 Measured maximum gain versus frequency of two ports of U shape slot conformal patch antenna.

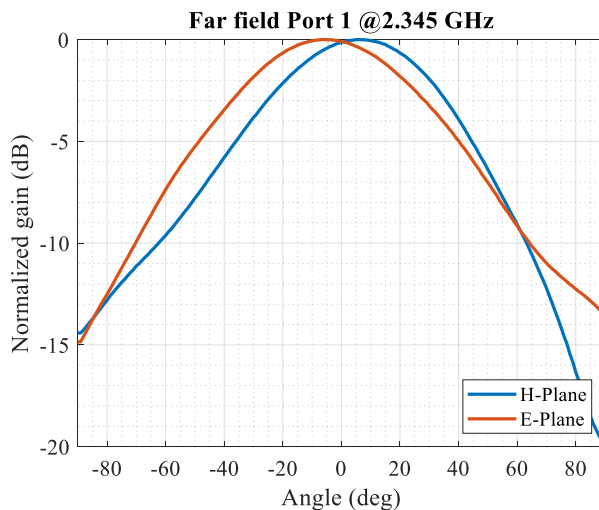


Fig. 29 Normalized measured radiation pattern of port one at central frequency of b40 band of U shape slot conformal patch antenna.

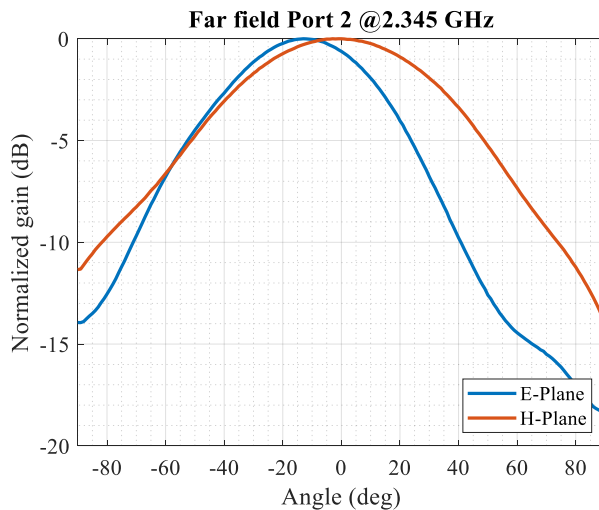


Fig. 30 Normalized measured radiation pattern of port two at central frequency of b40 band of U shape slot conformal patch antenna.

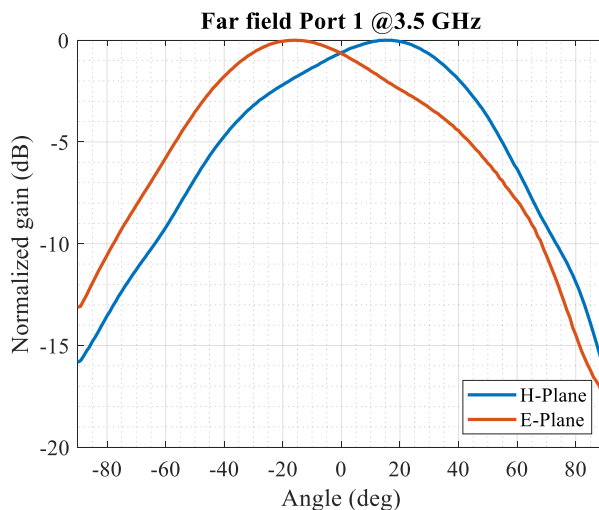
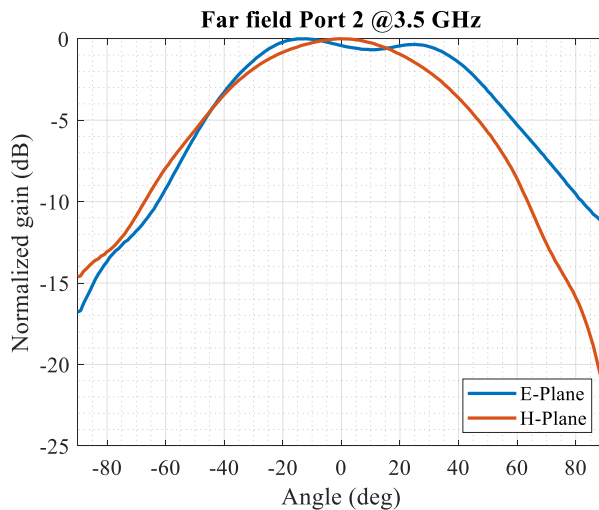


Fig. 31 Normalized measured radiation pattern of port one at central frequency of b42 band of U shape slot conformal patch antenna.

This measurement results shows that this last version of conformal patch antennas that is with "U" shape slots, are the best candidate of the designed antennas, due to multiband coverage, with an invariant polarization per port and feasibility to prototype it.



*Fig. 32 Normalized measured radiation pattern of port two at central frequency of b42 band of U shape slot conformal patch antenna.*

## 2.2 Mm-wave phased array patch antenna as reflector feed

### 2.2.1 Phased array patch antenna.

First, a 1x4 patch array antenna was designed to operate at the central frequency of 28 GHz. In addition, three different microstrip feed array were designed with phase shift of 0, 30 and 60 degrees to feed the patch antenna array. With these designed feeds, it is possible to obtain a main beam direction of 0, 8 and 17 degrees, as shown in Fig. 33. In a real scenario, the reflector will be feed by an electronically beam steered patch array. The use of these three examples emulates some cases of the real scenario with electronical beam steering.

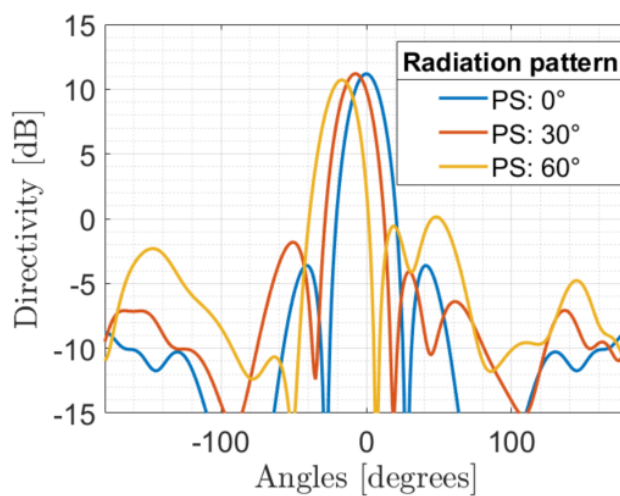


*Fig. 33 Simulated radiation pattern of the phased array patch antennas.*

These antennas were prototyped using computer assisted milling. Fig. 34 shows two different unassembled phased array patch antennas and Fig. 35 shows an assembled version.



Fig. 34 Unassembled prototypes of phased array patch antennas.



Fig. 35 Assembled prototype of phased array patch antenna.

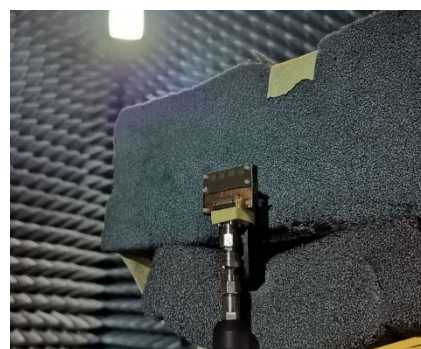
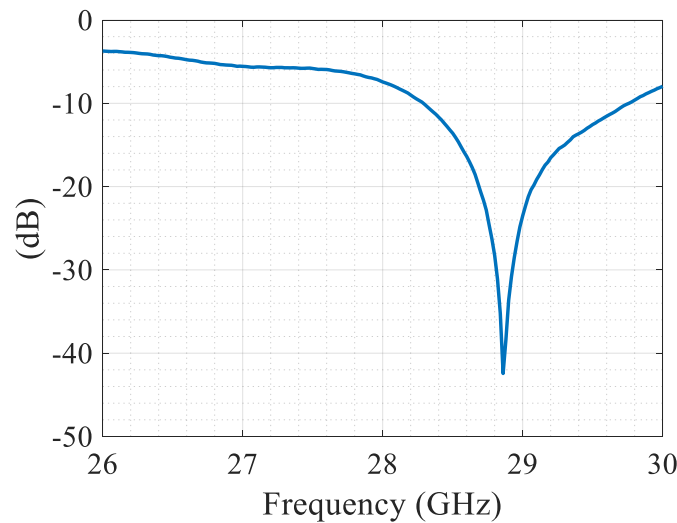
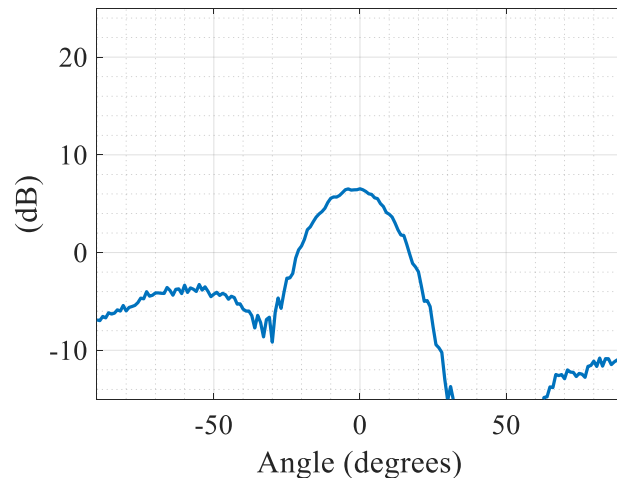


Fig. 36 Photo of measuring process of phased array patch antenna - 30° phase shift version.



*Fig. 37 Measured reflection coefficient of 30° phase shift of phased array patch antenna.*



*Fig. 38 Measured radiation pattern of 30° phase shift patch array at 26 GHz.*

To study whether they were well constructed, they were measured. First the phased array antenna with 30 degrees of phase shift was measured for its reflection coefficient, as shown in Fig. 37 where it can be seen that the resonance frequency is shifted. The second measurement was made on an anechoic chamber, to measure its far-field radiation pattern as shown in Fig. 38, Fig. 39 and Fig. 40 at 26, 28 and 30 GHz. Fig. 41 shows the maximum gain versus frequency between 26 and 40 GHz. From these figures, it can be seen that the maximum gain obtained is significantly lower than the simulation. At this point, it was necessary to know if these results were due to the manufacturing process or to the losses which are considerable for

microstrip technology at high frequencies. For this reason, we compare the normalized radiation pattern at the central frequency of 28 GHz, as shown in Fig. 42.

From this figure, it can be seen that the simulated and the measured radiation patterns have the same beam width, which mean that both have the same focusing capability, that is, the directivity. For this reason, we can conclude that the losses were high and the problem of adding air between the two layers of the antenna when they were assembled. For this reason, two different measurements have different maximum gain versus frequency plots (Fig. 41).

Analogously, this study was made for the phased array with 60 degrees of shift. Fig. 43, Fig. 44, Fig. 45, Fig. 46 show the same measured results than for the previous phased array, reaching the same conclusions.

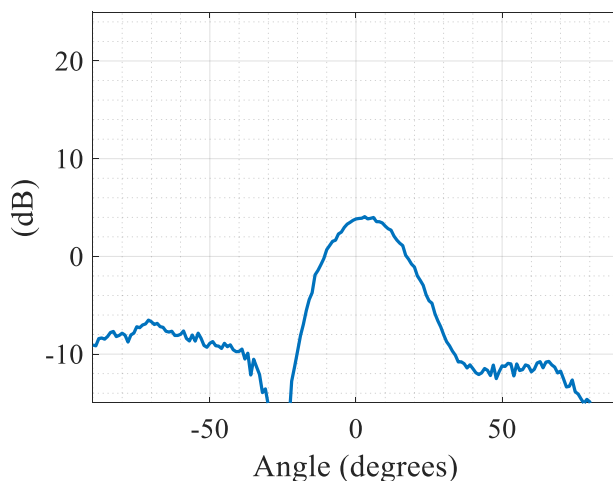


Fig. 39 Measured radiation pattern of 30° phase shift patch array at 28 GHz.

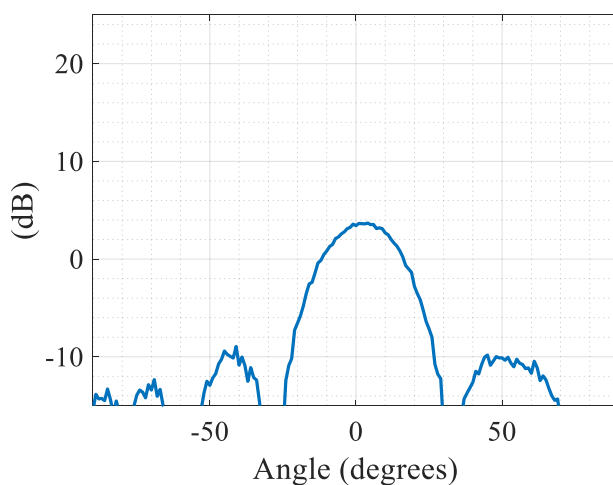


Fig. 40 Measured radiation pattern of 30° phase shift patch array at 30 GHz.

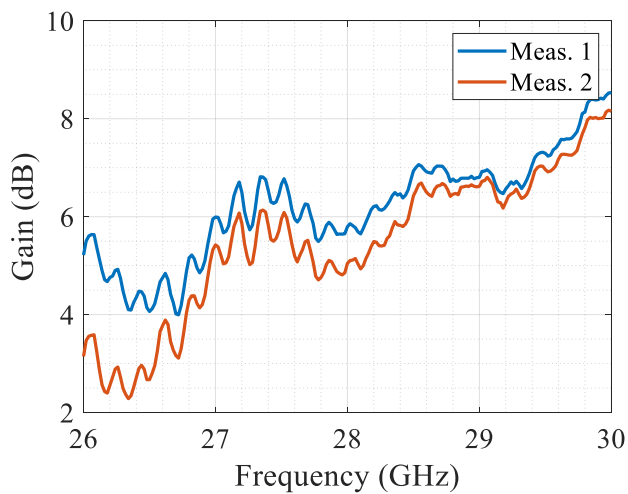


Fig. 41 Measured gain versus frequency of 30° phase shift phased array patch antenna.

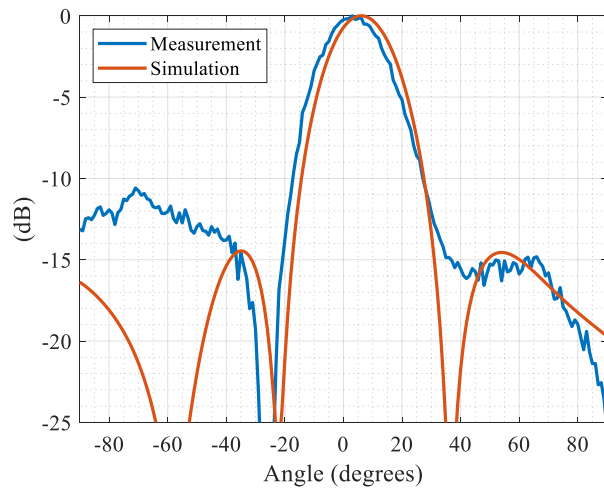


Fig. 42 Normalized measured and simulated radiation pattern of 30° phase shift phased array patch antenna at 28 GHz.

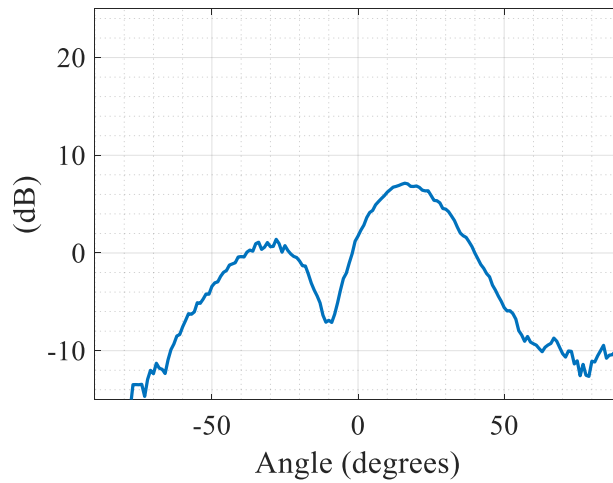


Fig. 43 Measured radiation pattern of 60° phase shift patch array at 26 GHz.

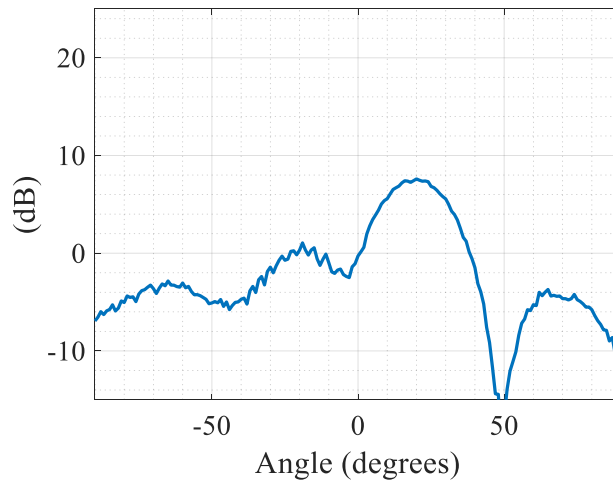


Fig. 44 Measured radiation pattern of 60° phase shift patch array at 28 GHz.

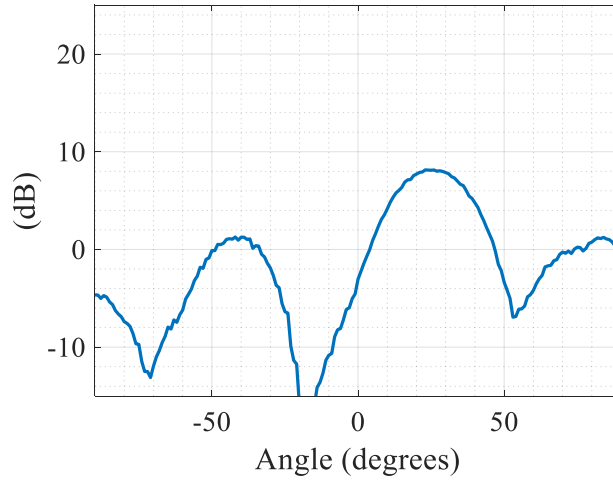


Fig. 45 Measured radiation pattern of 60° phase shift patch array at 30 GHz.

The next step was to measure the whole structure. To do this, it was necessary to assemble the phased array antenna with the reflector with its conformal patches. Fig. 47 shows the assembled antenna with its respective arm holding the phased array patch antenna jointly with the reflector with its conformal patches. Fig. 48 shows a back view of the whole structure where can be seen the SMA connectors to feed the sub-6 GHz conformal patches.

This antenna was placed on an anechoic chamber to measure its far field radiation pattern. Fig. 49, Fig. 50 and Fig. 51 show 3 different photos of this process.

The idea is to quantify the effect of adding the conformal patches in the reflectors surface.

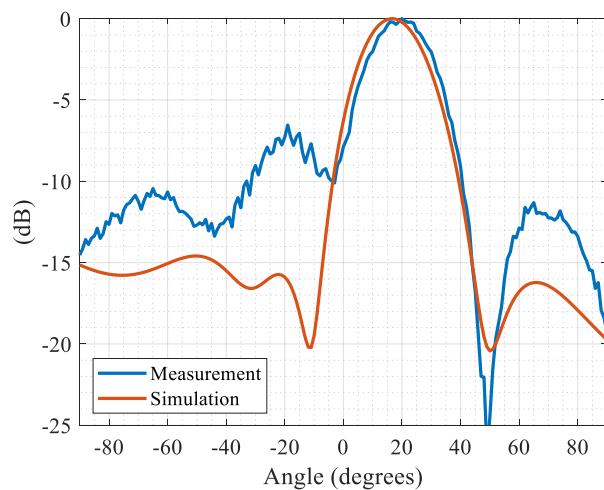


Fig. 46 Normalized measured and simulated radiation pattern of 60° phase shift phased array patch antenna at 28 GHz.

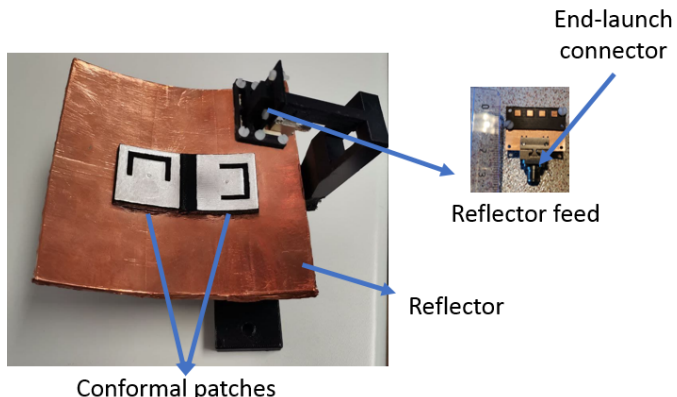


Fig. 47 Front view of U shape slot patch antennas conformal to the reflector fed by phased array patch antennas.

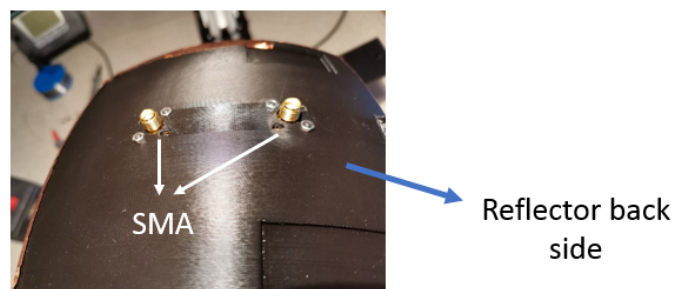


Fig. 48 Back view of U shape slot patch antennas conformal to the reflector fed by phased array patch antennas.

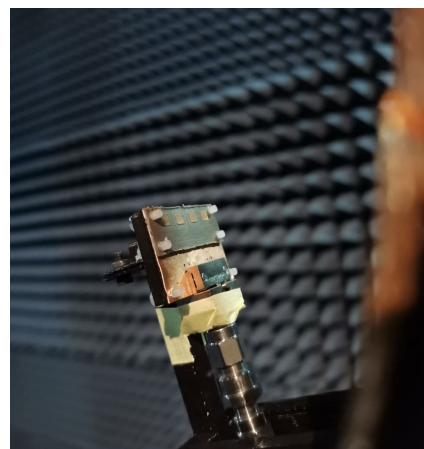
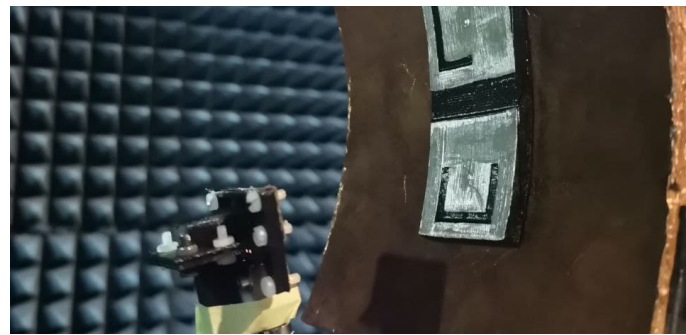


Fig. 49 Photo of measured prototype. Focus to phased array patch antenna.

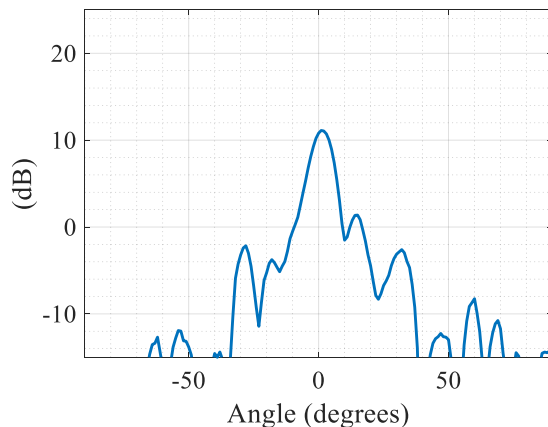


Fig. 50 Photo of measured assembled prototype.



*Fig. 51 Photo of measured assembled prototype.*

Fig. 52, Fig. 53 and Fig. 54 show the measured far-field radiation pattern produced by the reflector with conformal patches fed by the phased array antenna with 30 degrees of phase shift at 26, 28 and 30 GHz. It can be seen that all the diagram present a good focusing behavior, concluded by watching the beam width, but once again, the maximum gain of all of them is significantly lower than as expected, as can be seen in Fig. 55 from the comparison between the measured and simulated diagrams. To compare the focalizing properties of the reflector, Fig. 56 shown the normalized simulated and measured far-field radiation pattern. In this figure it can be seen that the beam width of both diagrams are almost the same, so it is possible to conclude that the directivity are the same in both cases, so the gain difference between the simulation and measurement is due losses in the feed.



*Fig. 52 Mm-wave measured radiation pattern of assembled prototype at 26 GHz. Feed of mm-wave patch array with phase shift of 30°.*

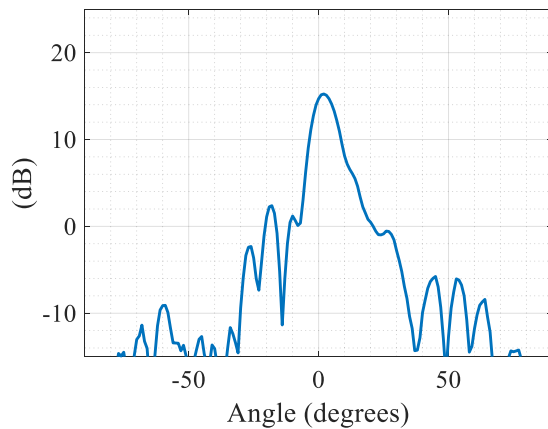


Fig. 53 Mm-wave measured radiation pattern of assembled prototype at 28 GHz. Feed of mm-wave patch array with phase shift of 30°.

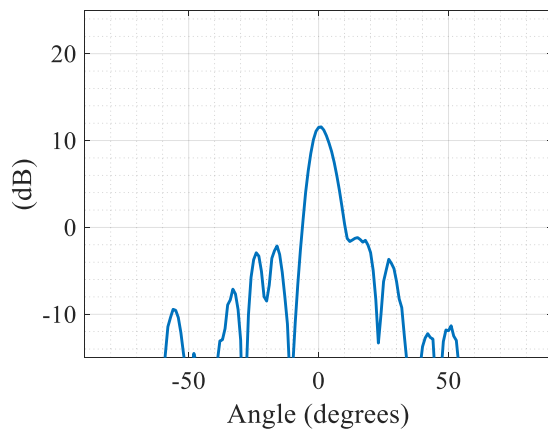


Fig. 54 Mm-wave measured radiation pattern of assembled prototype at 30 GHz. Feed of mm-wave patch array with phase shift of 30°.

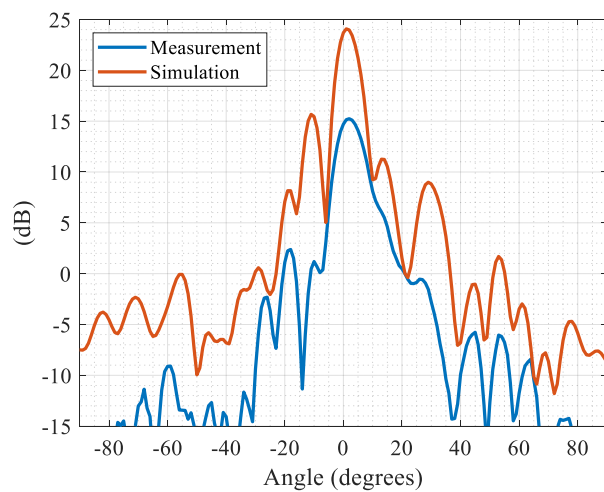
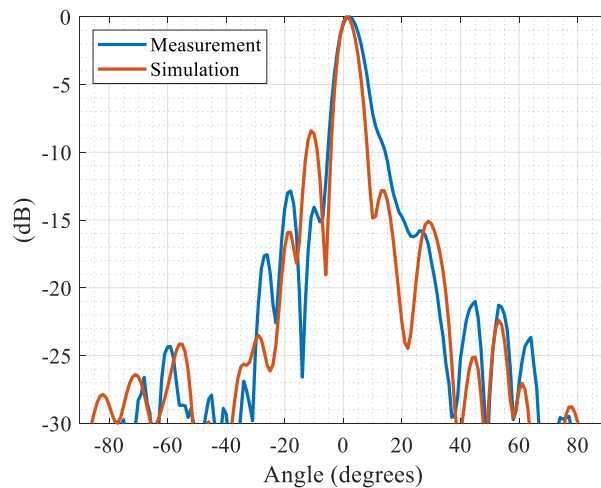


Fig. 55 Mm-wave measured versus simulated radiation pattern of assembled prototype at 28 GHz. Feed of mm-wave patch array with phase shift of 30°.

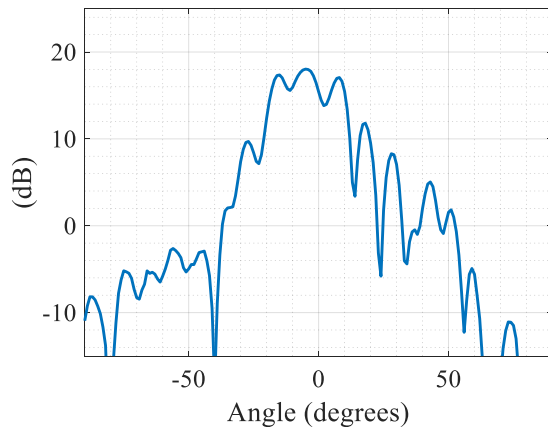


*Fig. 56 Mm-wave normalized measured versus simulated radiation pattern of assembled prototype at 28 GHz. Feed of mm-wave patch array with phase shift of 30°.*

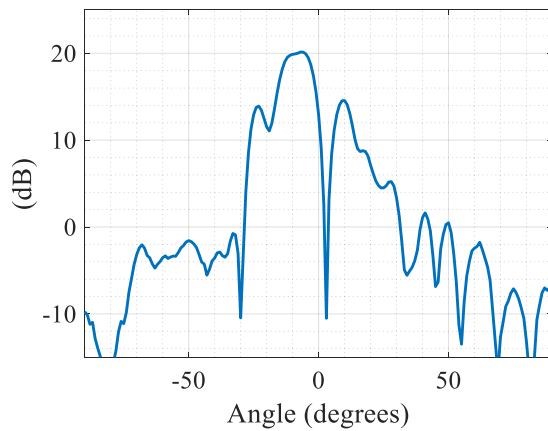
Analogously, Fig. 57, Fig. 58 and Fig. 59 shows the far-field radiation pattern produced by the reflector with conformal patches fed by the phased array, but in this case with 60 degrees of phase shift at 26, 28 and 30 GHz.

Fig. 60 shows the far field radiation patter simulated versus measured. It can be seen that in this case the gain differences are lower than the previous version. This is due to the fact that in this case the patch array with its microstrip network it is much better assembled, eliminating misalignments and air present between the layers.

From the normalized simulated and measured far-field radiation pattern of Fig. 61 it can be seen that in this case there is a slight deformation of the pattern produced by the conformal patches, but still the beam width is quite similar.



*Fig. 57 Mm-wave measured radiation pattern of assembled prototype at 26 GHz. Feed of mm-wave patch array with phase shift of 60°.*



*Fig. 58 Mm-wave measured radiation pattern of assembled prototype at 28 GHz. Feed of mm-wave patch array with phase shift of 60°.*

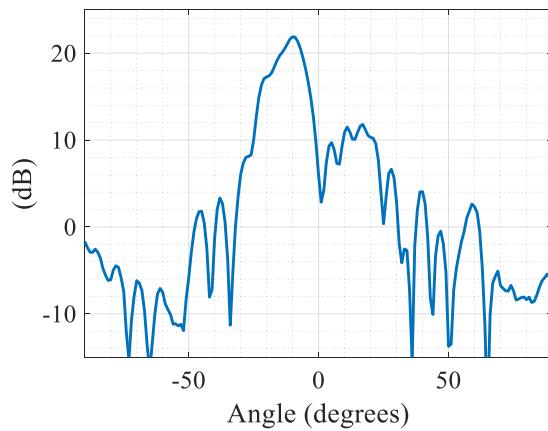


*Fig. 59 Mm-wave measured radiation pattern of assembled prototype at 30 GHz. Feed of mm-wave patch array with phase shift of 60°.*

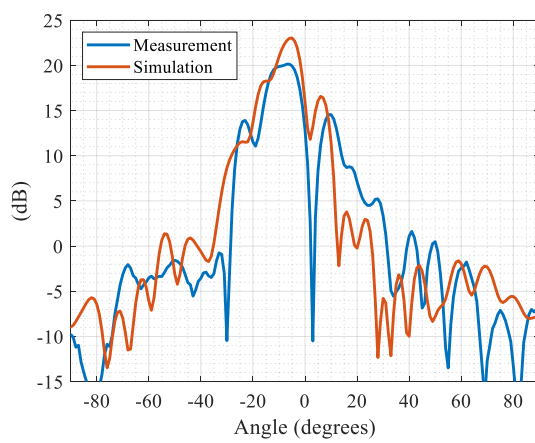


*Fig. 60 Mm-wave measured versus simulated radiation pattern of assembled prototype at 28 GHz. Feed of mm-wave patch array with phase shift of 60°.*

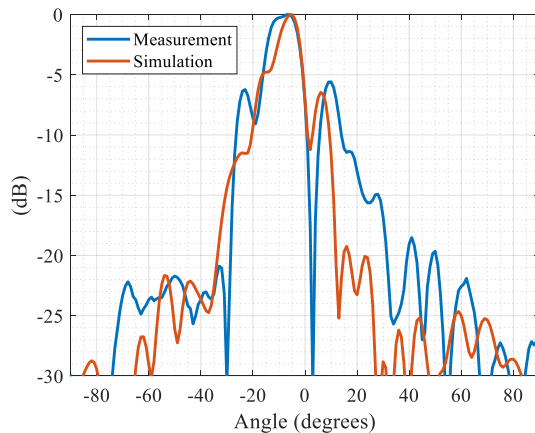


Fig. 61 Mm-wave normalized measured versus simulated radiation pattern of assembled prototype at 28 GHz. Feed of mm-wave patch array with phase shift of 60°.

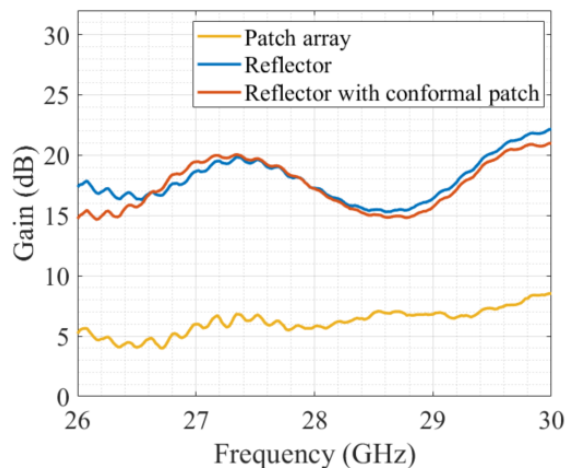
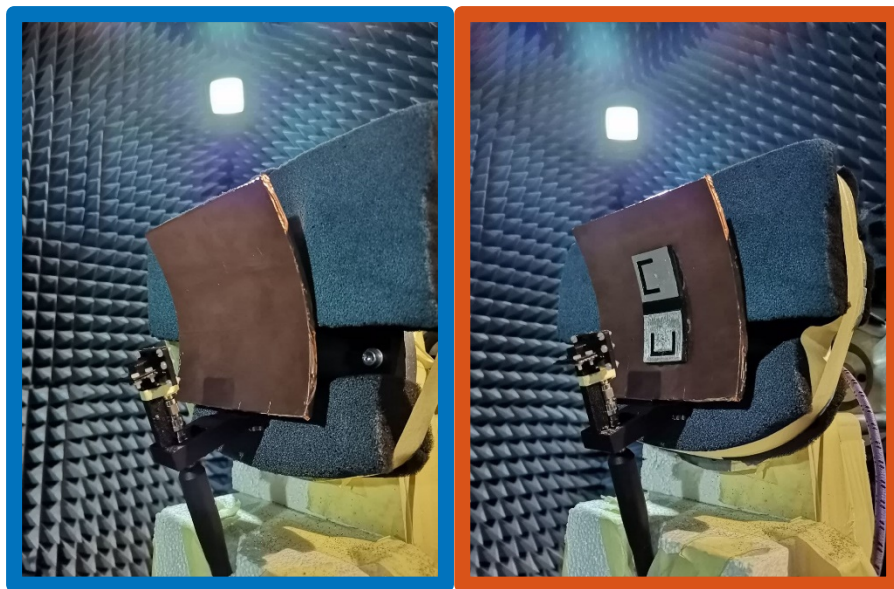
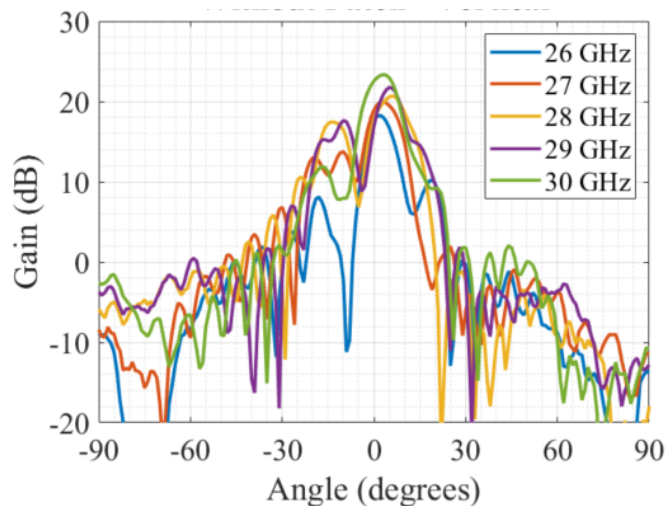


Fig. 62 Measured gain versus frequency of mm-wave phased array patch antenna with 60° of phase shift, reflector antenna fed phased array and reflector antenna with conformal patches fed by this phased array patch antenna.



*Fig. 63 Measured prototypes of reflector antenna fed by phased array patch antennas with 60° of phase shift without conformal patches (blue borders) and with conformal patches (red borders).*



*Fig. 64 Measured E-Plane radiation patterns of reflector with conformal patches prototype between 26 and 30 GHz. Phased array with 60° of phase shift.*

As mentioned above, a study of the effect on the millimeter-wave performance of adding the conformal patches on the reflector surface is required. For this, measurements of the phased array fed reflector were performed, in one case with the conformal patches on the reflector surface, and in another without the conformal patches. In Fig. 62 we can see the gain values achieved by the phased array, by the

reflector without conformal patches fed by this phased array and, finally, the reflector fed by this phased array but this time with the patches on its surface.

As it can be seen, the gain values achieved by the reflector with and without the conformal patches are practically the same for the entire frequency range studied. In Fig. 63 you can see a photograph of the measured prototypes here named.

In addition, the radiation patterns of the antenna with the conformal patches were measured in both planes in the frequency range studied, with a 1 GHz pass. Fig. 64 shows these radiation patterns in the E-plane and Fig. 65 in the H-plane. In addition, Fig. 66 and Fig. 67 show these same results but from the reflector without the conformal patches on its surface of both planes.

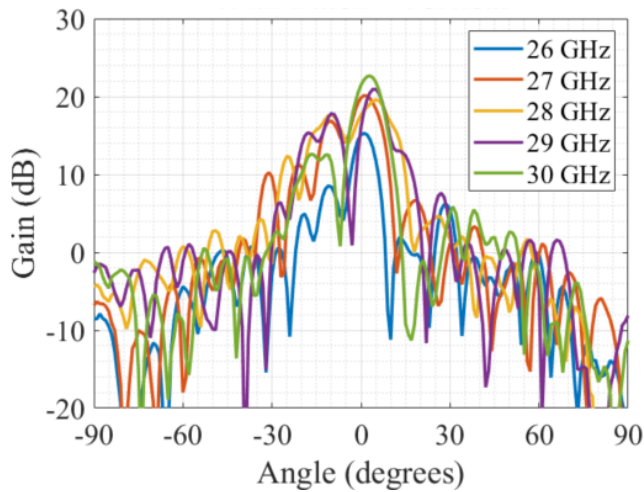


*Fig. 65 Measured H-Plane radiation patterns of reflector with conformal patches prototype between 26 and 30 GHz. Phased array with 60° of phase shift.*

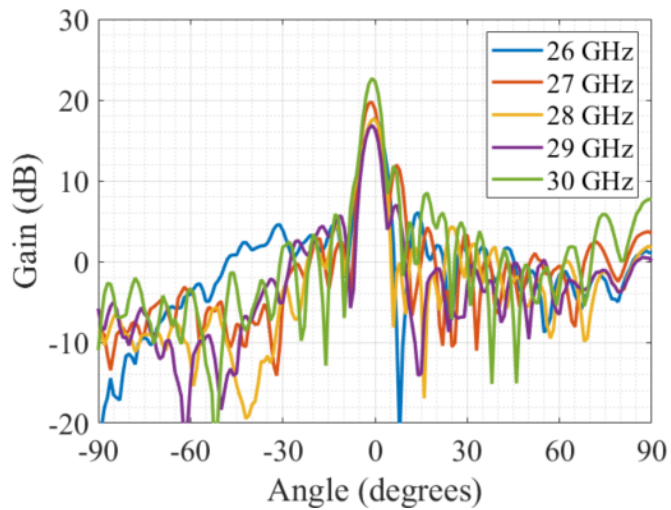


*Fig. 66 Measured E-Plane radiation patterns of reflector without conformal patches prototype between 26 and 30 GHz. Phased array with 60° of phase shift.*

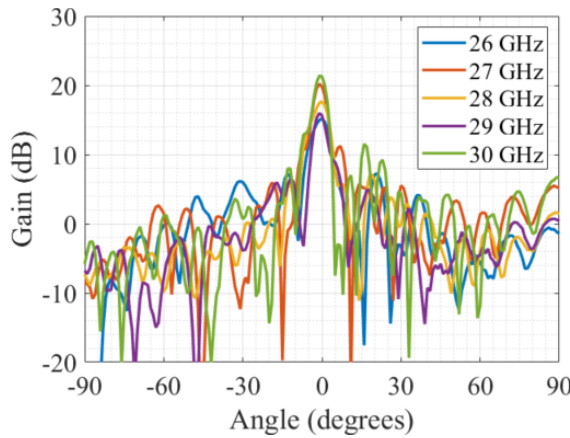


*Fig. 67 Measured H-Plane radiation patterns of reflector without conformal patches prototype between 26 and 30 GHz. Phased array with 60° of phase shift.*

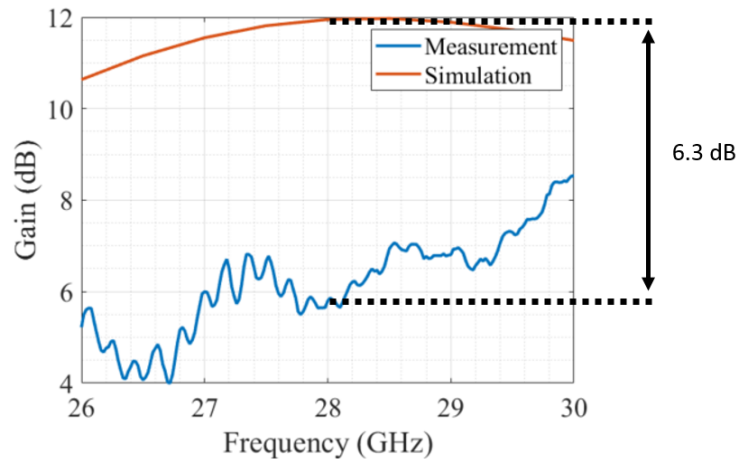


*Fig. 68 Measured and simulated gain versus frequency between 26 and 30 GHz of phased array patch antenna with 60° of phase shift.*

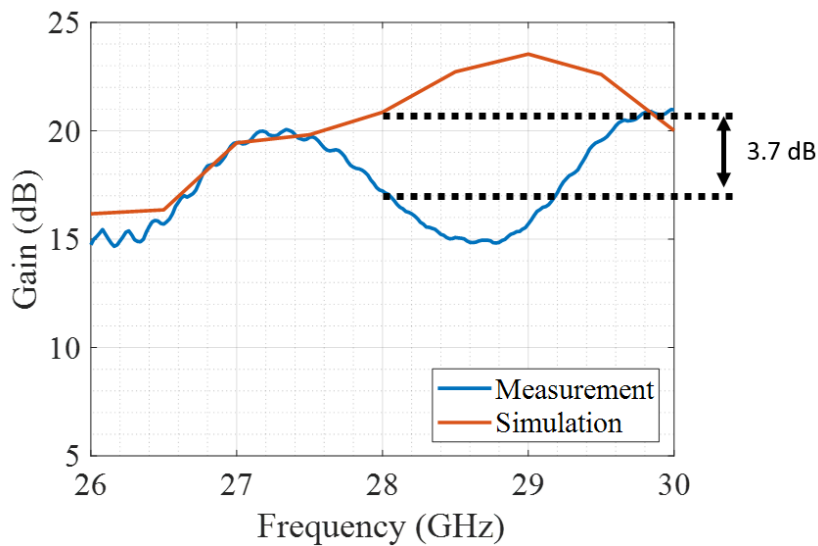


*Fig. 69 Measured and simulated gain versus frequency between 26 and 30 GHz of reflector antenna with conformal patches fed by phased array patch antenna with 60° of phase shift.*

Finally, Fig. 68 shows the gain versus frequency of the simulated and measured models of the phased array, which present an important difference. In the other hand, Fig. 69 shows the gain versus frequency of the simulated and measured assembled model of the reflector antenna with conformal patches. The conclusion is that the feeding phased arrays introduces much more losses than in simulation.

# 3 Channel characterization measurements for beamforming strategies

## 3.1 Indoor-indoor channel measurement

For the channel characterization measurement, first we select one scenario, which plane is shown in Fig. 70. These measurements will be done with a Vector Network Analyzer (VNA), connecting to one port the transmission antenna with a fixed angle (red dots in Fig. 70) and to the second port the receiver antenna. The transmission coefficient will be measured between these both antennas, at different angles in the top half-sphere. The blue dots represent the different positions where the receiver antenna will be positioned. To avoid measurement error and noise, it has been decided to measure fifteen times at each angle and then average these values. In addition, it was decided to normalize the measurements with respect to the highest relative receiver power values.

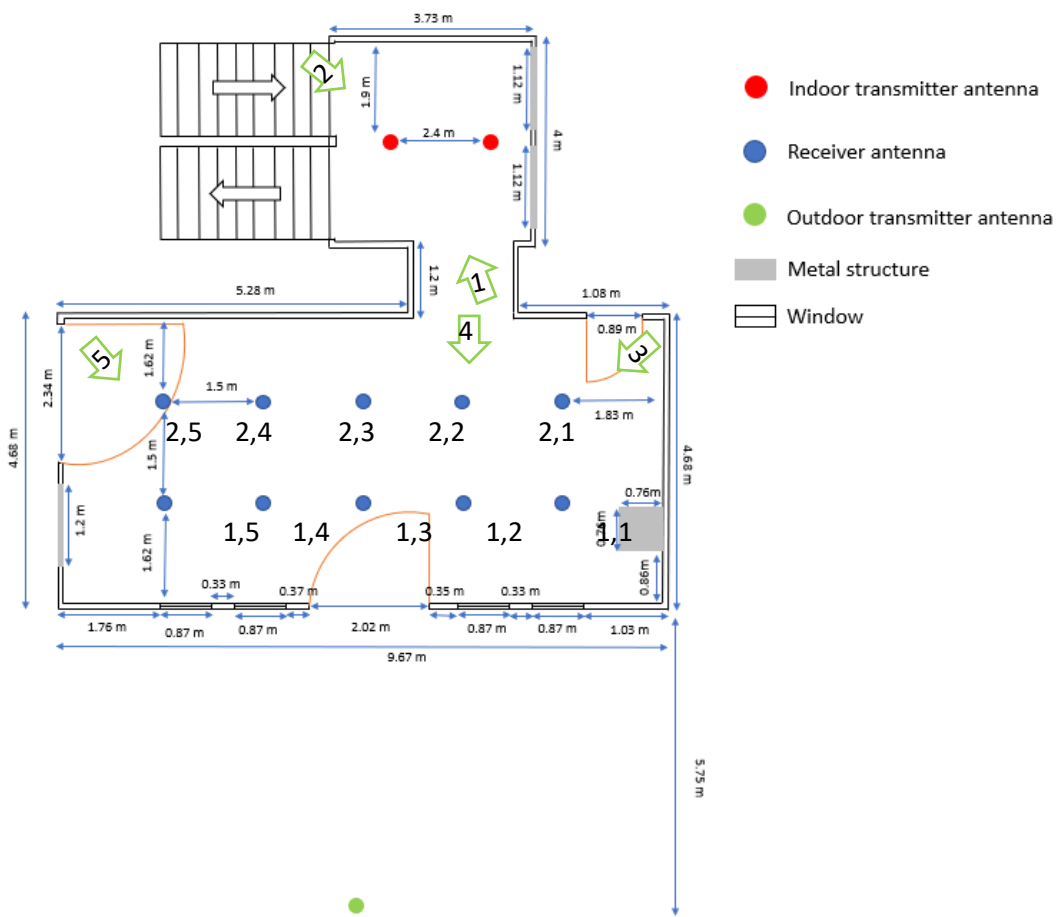


Fig. 70 Indoor-indoor measurement and first indoor-outdoor measurement scenario plan.

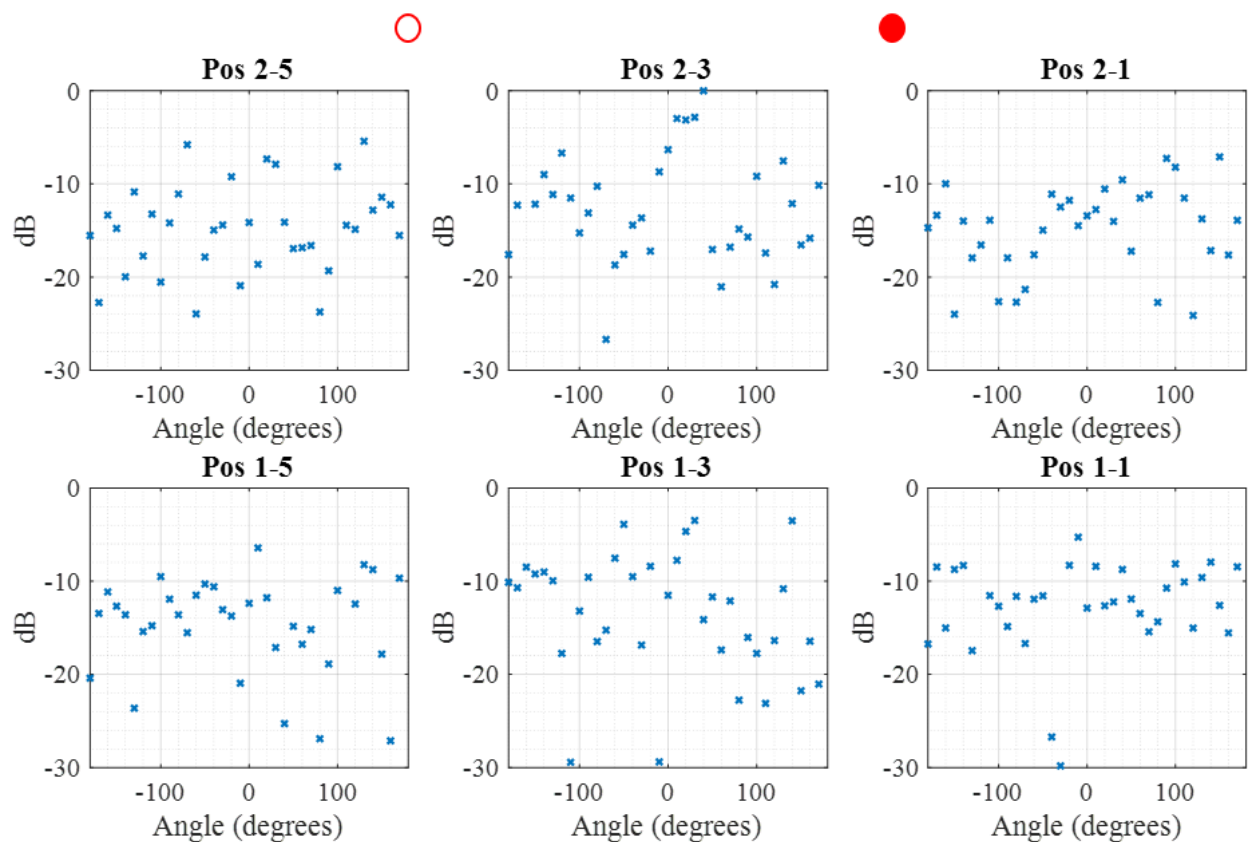


Fig. 71 Indoor-indoor channel measurement results between right transmitter antenna and receiver antenna at six different positions. Azimuthal rotation.

Fig. 71 shows the measurement results of normalized relative power received at the different angles for the six different positions, with the transmitter antenna positioned at the right side, represented by the red dot at the top of this figure. It can be seen that the maximum relative power is reached when the receiver antenna is in the (2,3) position, with forty degrees as expected, pointing to the transmitter antenna, that is, line of sight (LOS).

Another important result of these measurements is that it can be observed that there is no single dominant ray for all positions. For example, for the position (1,3) there are three dominant rays with practically the same power levels, separated by approximately fifty degrees from each other.

Fig. 72 shows an elevation cut in the azimuthal angle with higher relative power. For example for position (2,3), the cut is done in forty degrees and for position (1,5) is done in ten degrees. From these results, one important conclusion is that it is possible to receive more power when pointing the antenna to higher angles.

It is important to say that the conclusions for the other measurement done analogue, presented in Fig. 73 and Fig. 74, with the difference that the angles are different because the angles between the antennas are different. For example, in this case the maximum relative transmitted power occur at the position (2,1), when the antennas are pointing to each other.

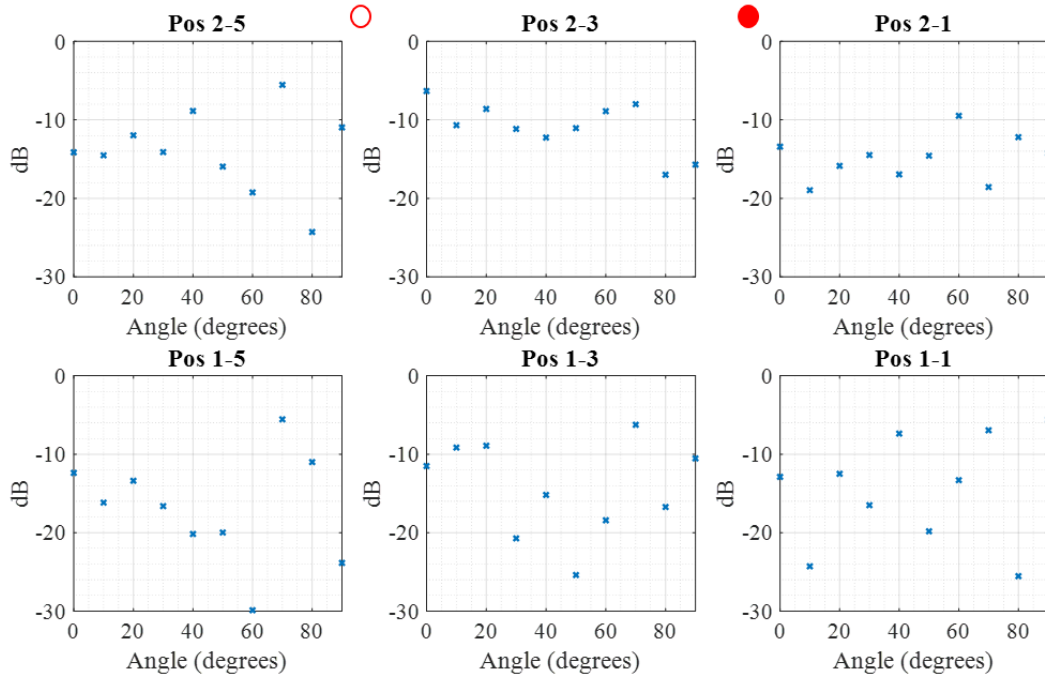
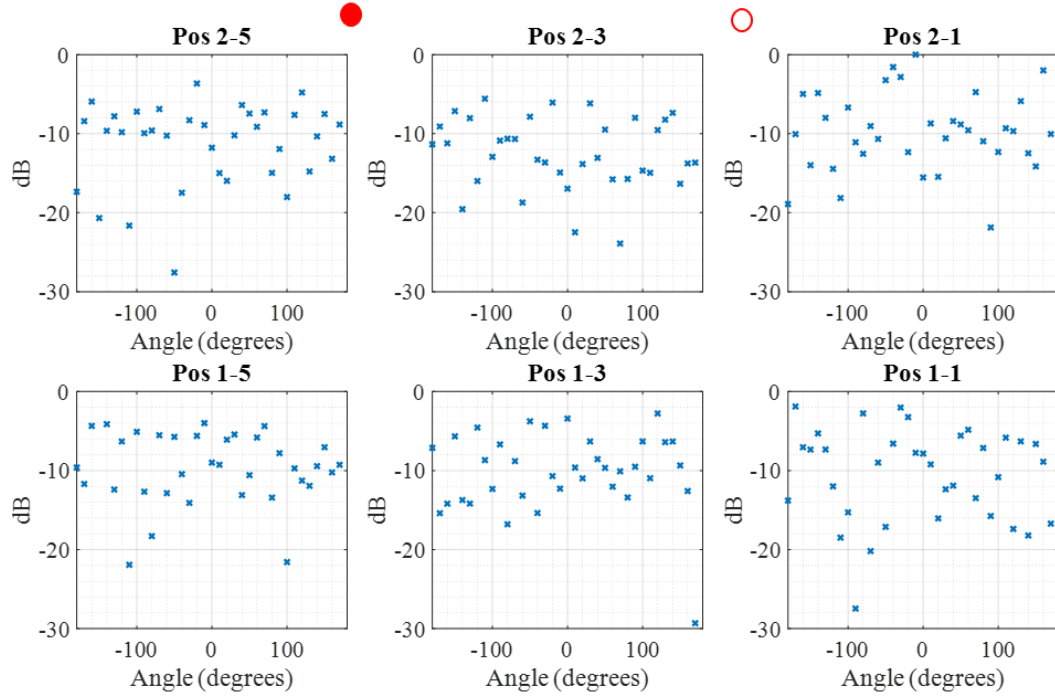
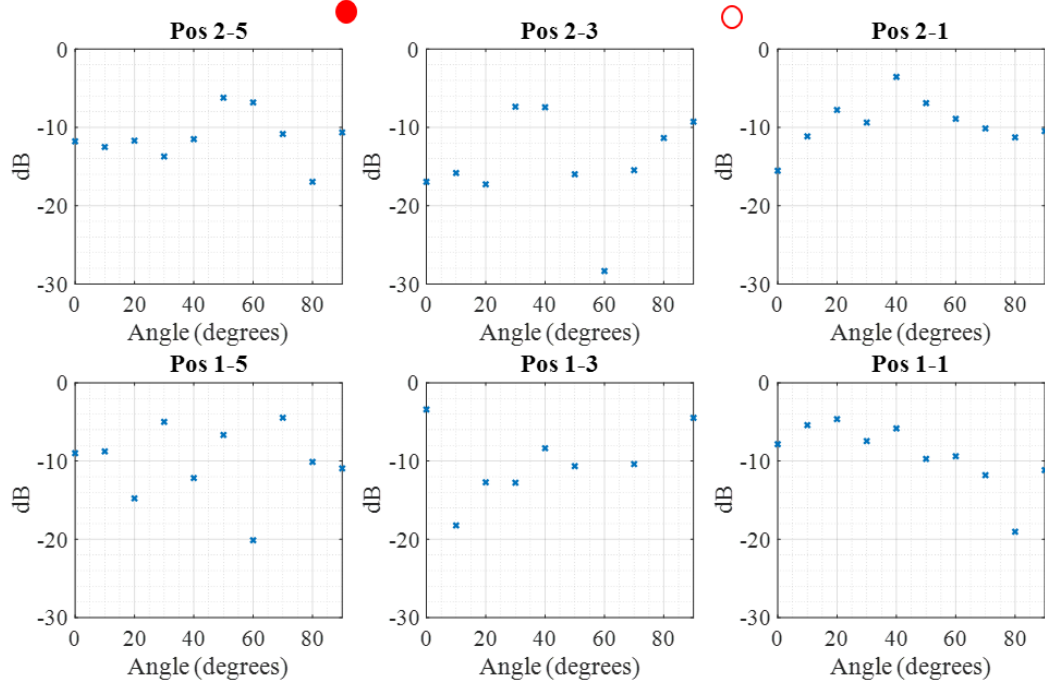


Fig. 72 Indoor-indoor channel measurement between right transmitter antenna and receiver antenna at six different positions. Elevation rotation at highest measured power in azimuthal of each position.



*Fig. 73 Indoor-indoor channel measurement results between left transmitter antenna and receiver antenna at six different positions. Azimuthal rotation.*



*Fig. 74 Indoor-indoor channel measurement between left transmitter antenna and receiver antenna at six different positions. Elevation rotation at highest measured power in azimuthal of each position.*



## 3.2 Indoor-outdoor measurements

As explained in [2], indoor-outdoor measurement for channel characterization were performed, as this is a more realistic scenario and it is critical to analyze the received signal inside for different angles when the emitted signal comes from outside.

### 3.2.1 First scenario

#### 3.2.1.1 Same height both antennas

The first measurement of this scenario was with both antennas with the same height. Fig. 75 shows the azimuthal measurement results with the receiver antenna at ten different positions. In the same way than for the previous measurements, here it was measured the transmission coefficient between the transmitter, positioned in the outside in this case, and the receiver which rotates to measure a half of the sphere, at ten different positions.

From this figure, it can be seen that the global maximum is in the position (1,3) at 0 degrees. This is an expected result because the antennas are in LOS.

Fig. 76 shows the elevation measurement at the maximum azimuthal position. For a better view of the results, Fig. 77 shows the same results than Fig. 75 but in a polar plot. There are two important lines on this graph. The first one is the solid red line that points to the receiving antenna, in order to have a reference of in which direction it is located. The second is the dotted black line. This points in the direction of the highest relative power in the azimuthal plane with zero degrees of elevation. This allows a better reading of the data.

For example, for position (1,3), the maximum in the azimuthal plane at zero degrees of elevation is in the same direction as the transmitting antenna. This is an expected result since both are facing each other. This result is repeated for positions (2,3) and (1,4).

On the other hand, for all the other situations, it happens that the maximum in this plane is not found when the receiving antenna is pointing towards the transmitting antenna, but due to some bouncing that occurs inside the room. There are some more extreme cases in which the maximum is 160 degrees off the physical angle between the two antennas, as occurs in position (2,1).

It is important to emphasize that these situations depend on the physical characteristics of the measured room. For example, in this particular room there are some metal areas that facilitate the reflection of energy in some specific directions.

Fig. 78 shows a photograph of the measurement setup at this scenario. It can be seen the transmitter antenna at the outside, the receiver antenna placed at the mechanical rotation system in (1,3) position, the VNA and the personal computer.

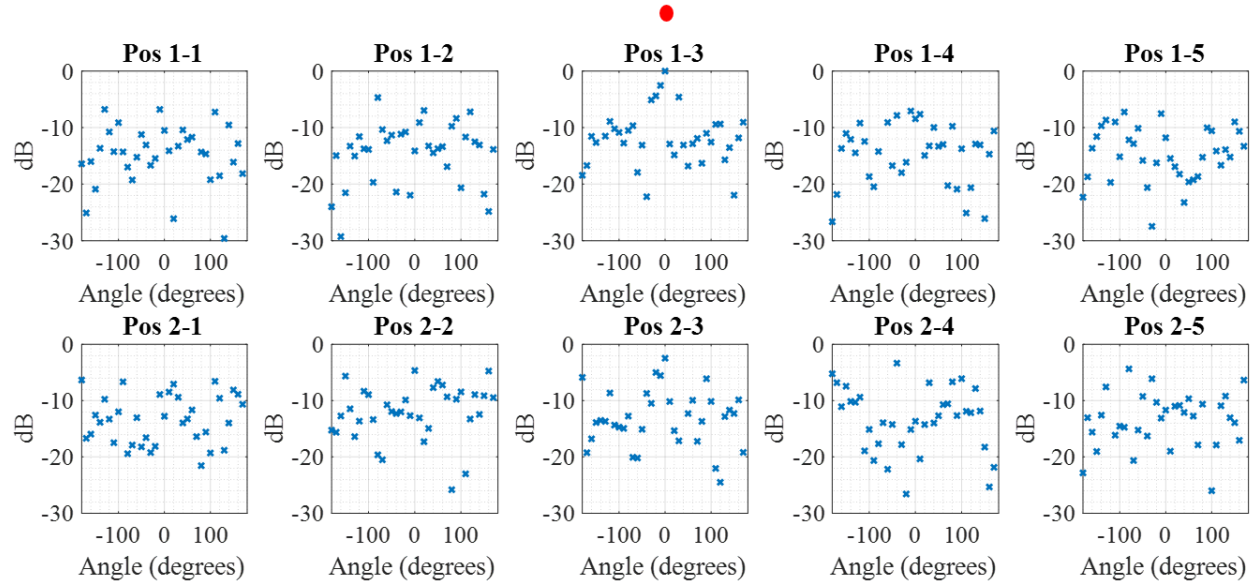


*Fig. 75 Indoor-outdoor channel measurement results between transmitter antenna and receiver antenna at ten different positions. Azimuthal rotation.*

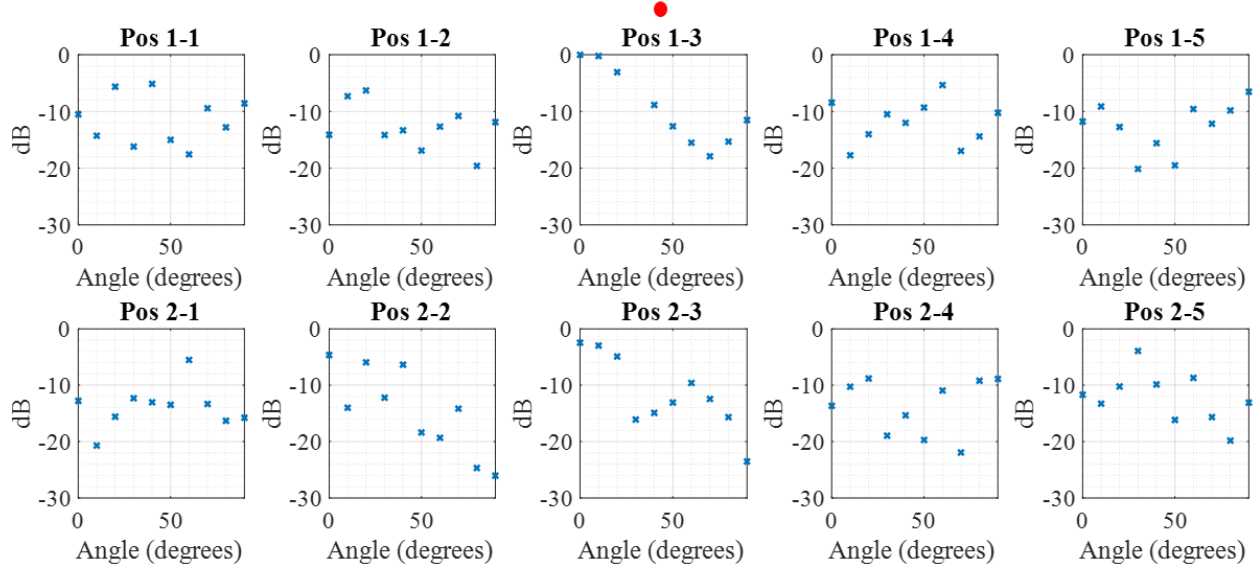


*Fig. 76 Indoor-outdoor channel measurement between transmitter antenna and receiver antenna at ten different positions. Elevation rotation at highest measured power in azimuthal of each position.*

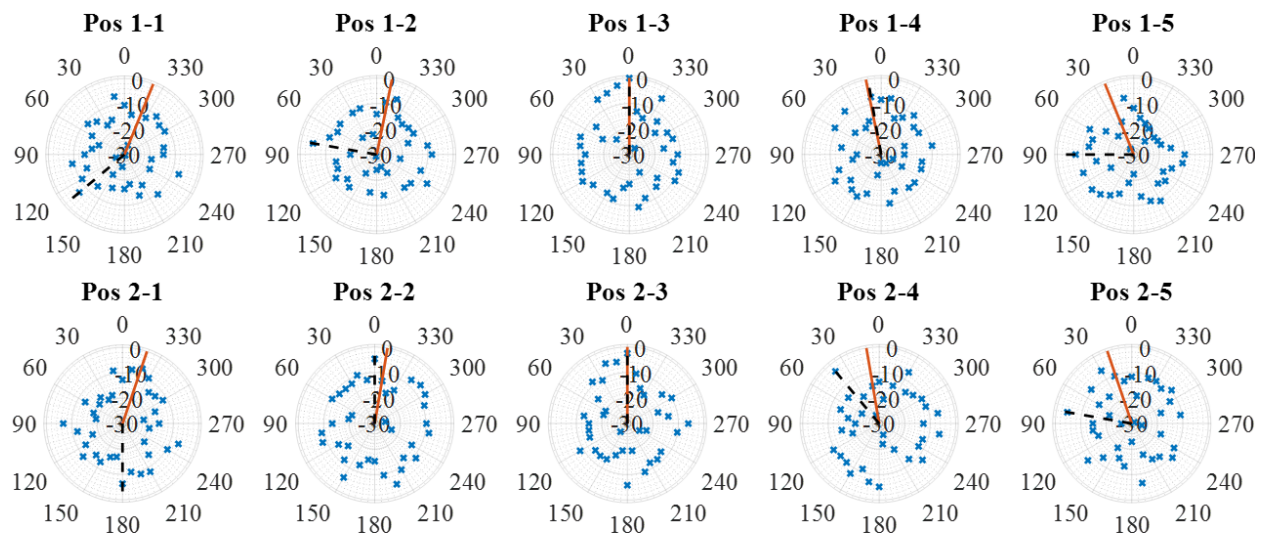


*Fig. 77 Indoor-outdoor channel measurement polar results between transmitter antenna and receiver antenna at ten different positions. Azimuthal rotation. Red line: physical angle between receiver and transmitter antenna. Black dotted line: direction of maximum power.*



*Fig. 78 Indoor-outdoor measurement scenario and setup photograph.*

Finally, Fig. 79 shows the elevation measurement in a polar plot. From this graph an important conclusion is that for almost all positions, it is possible to get the maximum received relative power with a scanning of thirty degrees.

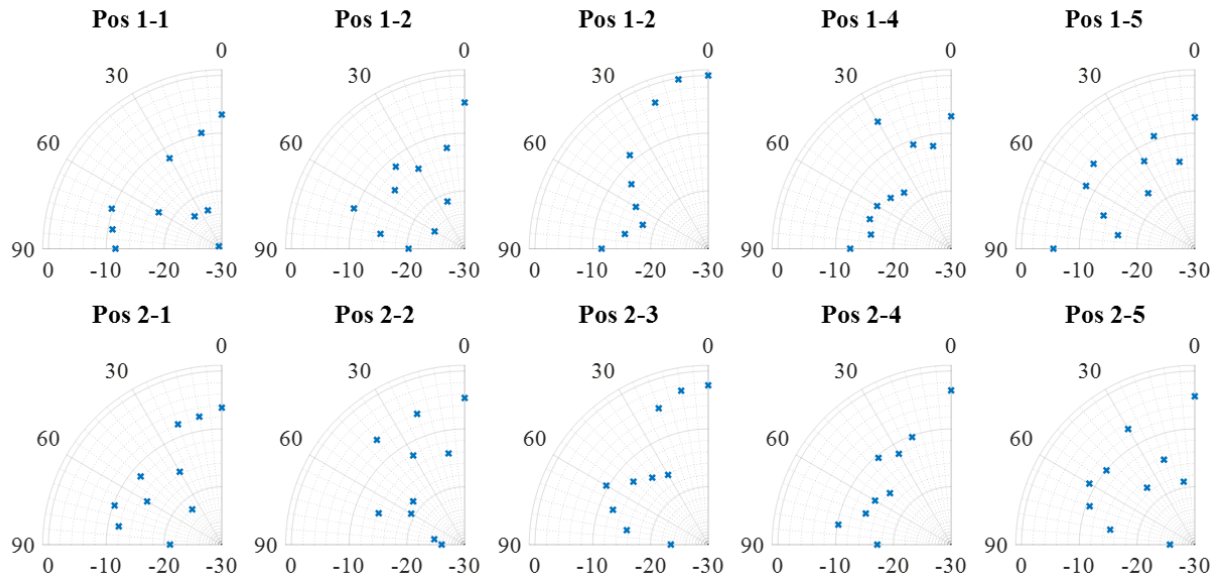


Fig. 79 Indoor-outdoor channel polar measurement between transmitter antenna and receiver antenna at ten different positions. Elevation rotation at highest measured power in azimuthal of each position.

### 3.2.1.2 Both antennas with different height.

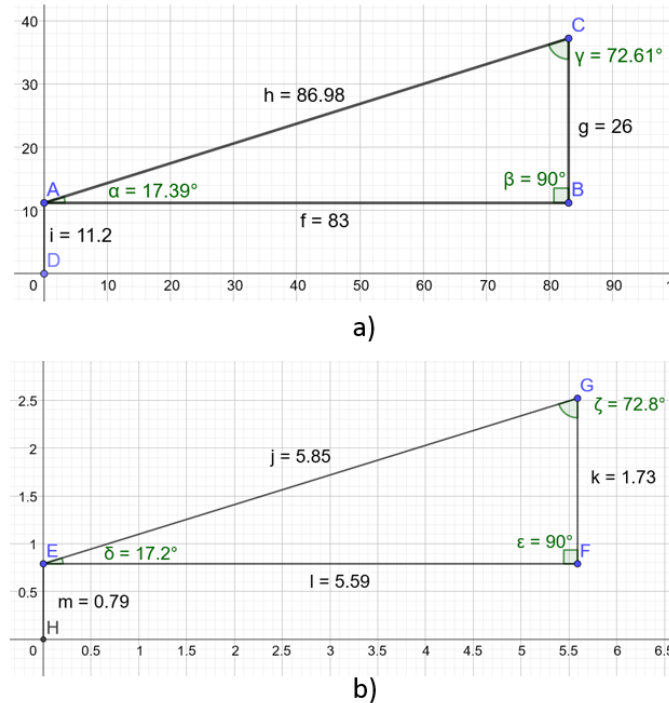
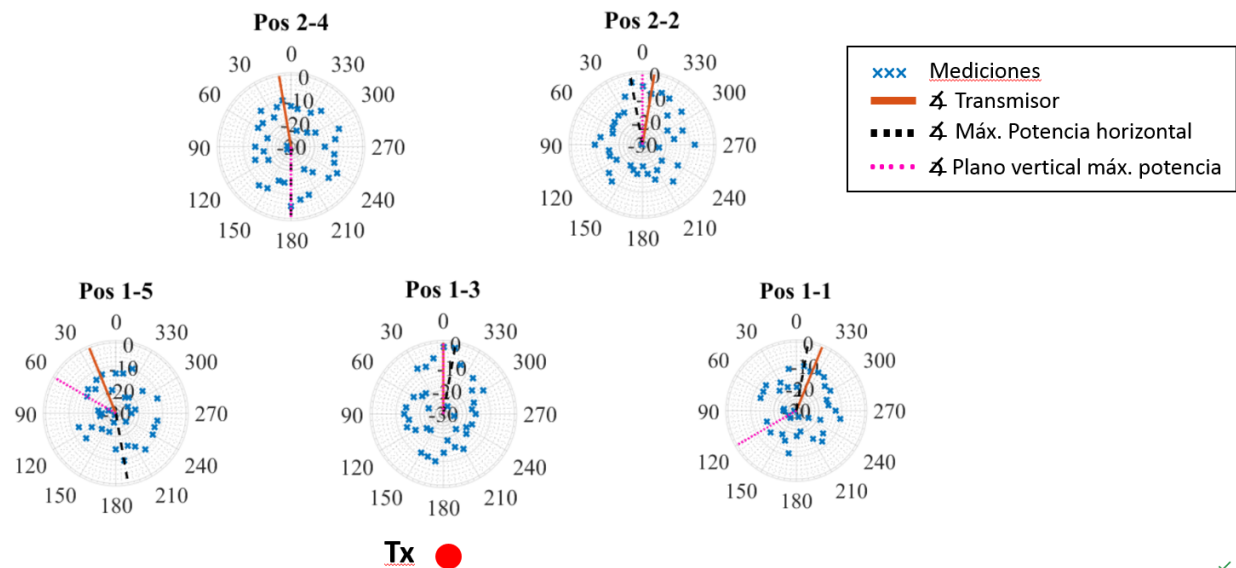


Fig. 80 Angular and height difference between transmitter and receiver antennas diagram. Top: realistic case. Bottom: implemented case.

In the same scenario, a second set of measurement were done. In this case, the antennas were placed with a height difference and the transmitter antenna with a declined angle, as explained in Fig. 80.

For this more realistic scenario, we found that in most cases, the global maximum of the hemisphere was not the same as the maximum of the azimuthal plane at zero degrees elevation, which was an expected result due to the transmitting antenna being at a higher altitude and pointing diagonally downward.

In Fig. 81 the measurement results can be seen, where the receiving antenna was positioned at five different positions in the chosen scenario. In these measurements there is a new dashed pink line, which points to the horizontal angle at which the global maximum of the hemisphere of that position is located.



*Fig. 81 Indoor-outdoor channel measurement polar results between transmitter antenna and receiver antenna at five different positions with different height. Azimuthal rotation. Red line: physical angle between receiver and transmitter antenna. Black dotted line: direction of maximum power. Pink dotted line: direction of maximum global power of each position.*

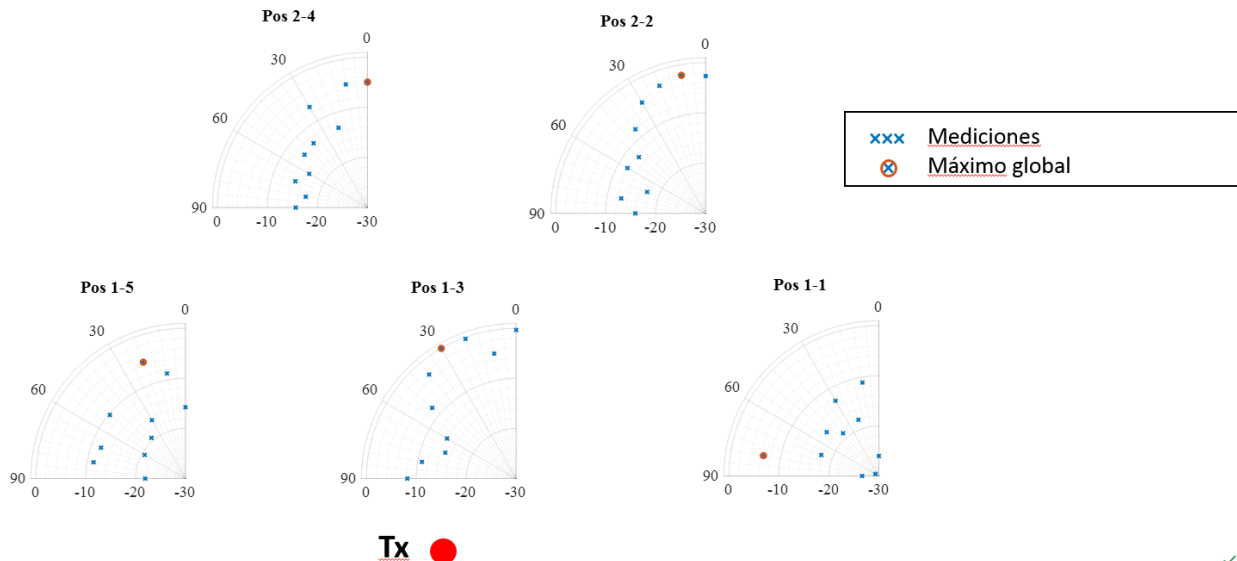


*Fig. 82 Indoor-outdoor channel polar measurement between transmitter antenna and receiver antenna at five different positions. Elevation rotation at highest measured global power of each position. Red circle: maximum global power of each position.*

Fig. 82 shows the measurement results in the elevation plane. It is important to note that this time the measurements were performed in the plane indicated by the dotted pink line in each of the positions, i.e., where the global maximum of the hemisphere was located.

An important conclusion drawn from this graph is that in four of the six different cases, with only thirty degrees of elevation it is possible to detect the maximum value of relative received power. In fact, the maximum of all positions, i.e., the value with which the values were normalized in these plots, is found just at thirty degrees of elevation at the position (1,3).

### 3.2.2 Second scenario

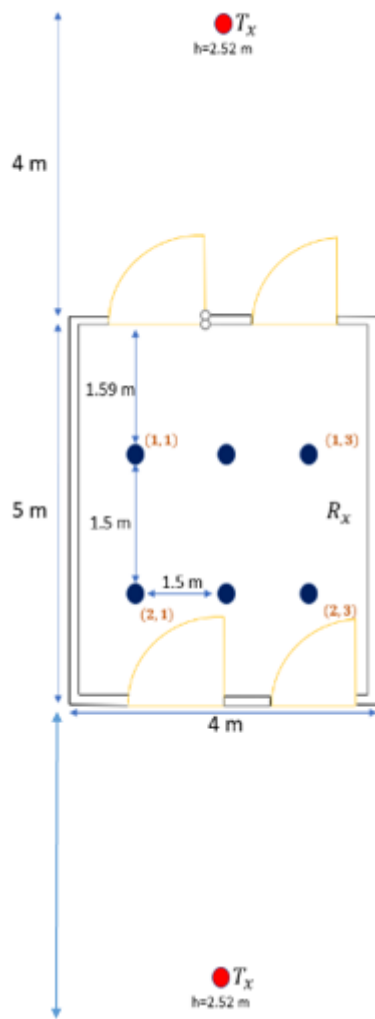
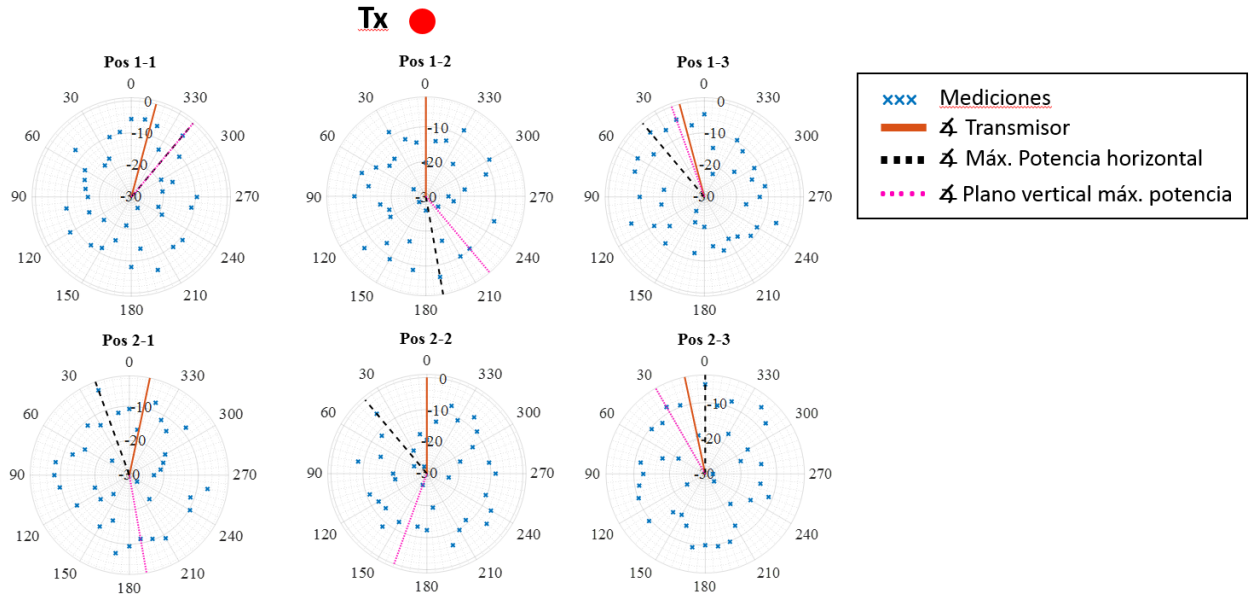
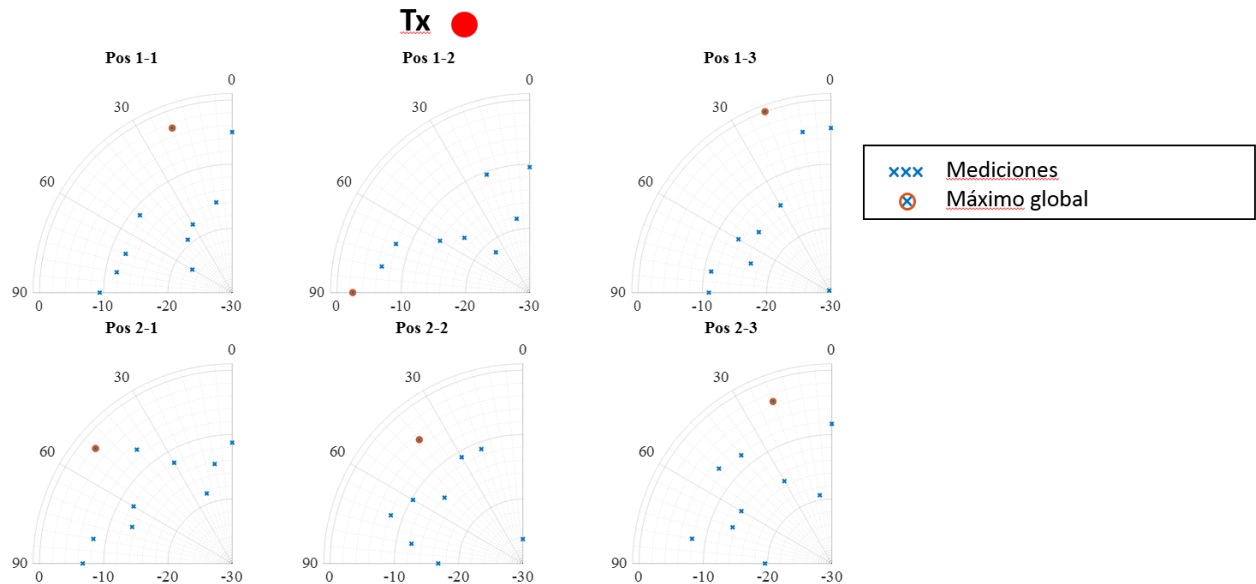


Fig. 83 Second indoor-outdoor measurement scenario plan.

After finishing the previous measurements, a second scenario was chosen in which to repeat these measurements, considering the situation in which both antennas are at different heights. This was decided in order to analyze if the conclusions obtained from the first measurement campaign could be generalized to other scenarios, or if they were particular to the one previously chosen. The description of this scenario is shown in Fig. 83. It can be seen that this selected scenario is smaller than the previous one, so only six different positions have been chosen where the receiving antenna will be placed, in order to maintain the distance between positions, that is, 1.5m.



*Fig. 84 Second scenario of indoor-outdoor channel measurement polar results between transmitter antenna and receiver antenna at six different positions with different height. Azimuthal rotation. Red line: physical angle between receiver and transmitter antenna. Black dotted line: direction of maximum power*



*Fig. 85 Second scenario indoor-outdoor channel polar measurement between transmitter antenna and receiver antenna at six different positions. Elevation rotation at highest measured global power of each position. Red circle: maximum global power of each position.*

Continuing with the procedure explained above, Fig. 84 shows the measurements in the azimuthal plane with zero degrees of elevation, for the six different positions in which the receiving antenna was placed. These plots show the same three lines as for the previous scenario: the solid red line pointing in the direction of the

transmitting antenna; the dotted black line pointing to the angle at which the highest relative power received from this azimuthal plane is located; and finally, the dotted pink line pointing in the direction of the highest overall relative power, i.e., of the entire hemisphere. Fig. 85 shows the elevation plane measurement results, in the plane where the highest relative power value of the hemisphere of each position is located.

Although this scenario is quite different from the previous one, especially since it does not present large metallic structures, it can be analyzed that the maximum relative power received can be found again within thirty degrees of vertical scanning.

Finally, Fig. 86, Fig. 87, Fig. 88, Fig. 89 and Fig. 90 show photographs taken in different positions of the chosen scenarios. In the caption of each one of them it is explained from which place of the scenery they were taken, making reference to the previously illustrated plan.



Fig. 86 Transmitting antenna positioning room for indoor-indoor measurements. Photo taken from the [green arrow number 1](#) shown in **iError! No se encuentra el origen de la referencia..**



Fig. 87 Transmitting antenna positioning room for indoor-indoor measurements. Photo taken from the [green arrow number 2](#) shown in **iError! No se encuentra el origen de la referencia..**



Fig. 88 Receiving antenna positioning room for indoor-indoor and indoor-outdoor measurements. Photo taken from the [green arrow number 3](#) shown in **iError! No se encuentra el origen de la referencia..**



Fig. 89 Receiving antenna positioning room for indoor-indoor and indoor-outdoor measurements with view to the outdoor area where the transmitting antenna of these measurements will be positioned. Photo taken from the [green arrow number 4](#) shown in **iError! No se encuentra el origen de la referencia..**



*Fig. 90 Receiving antenna positioning room for indoor-indoor and indoor-outdoor measurements with view to the outdoor area where the transmitting antenna of these measurements will be positioned. Photo taken from the [green arrow number 5](#) shown in **iError! No se encuentra el origen de la referencia..***

## 4 Subsystem integration and testing

In this last section of this deliverable the dual-band antenna described in Section 2.2 with the Mm-wave phased array patch antenna as reflector feed is used to identify if the propagation behaviour with the commercial antennas used in Section 3 is unchanged.

Measurements of both frequency bands are taken for the measurement scenario of Section 3.2.2.

### 4.1 Mm-wave channel measurement

Continuing with the measuring procedure from previous section, Fig. 91 shows the measurements in the azimuthal plane with zero degrees of elevation, for three different positions in which the receiving antenna was placed. These plots show the same two lines as for the previous scenarios: the solid red line pointing in the direction of the transmitting antenna; the dotted black line pointing to the angle at which the highest relative power received from this azimuthal plane is located.

Similarly to previous results, we observe a great dependence on the geometry of the room where the received antennas are placed, and in the positioning where the transmit antenna and receive antenna are in LOS (Pos 2-2) we receive a significant part of the transmitted power.

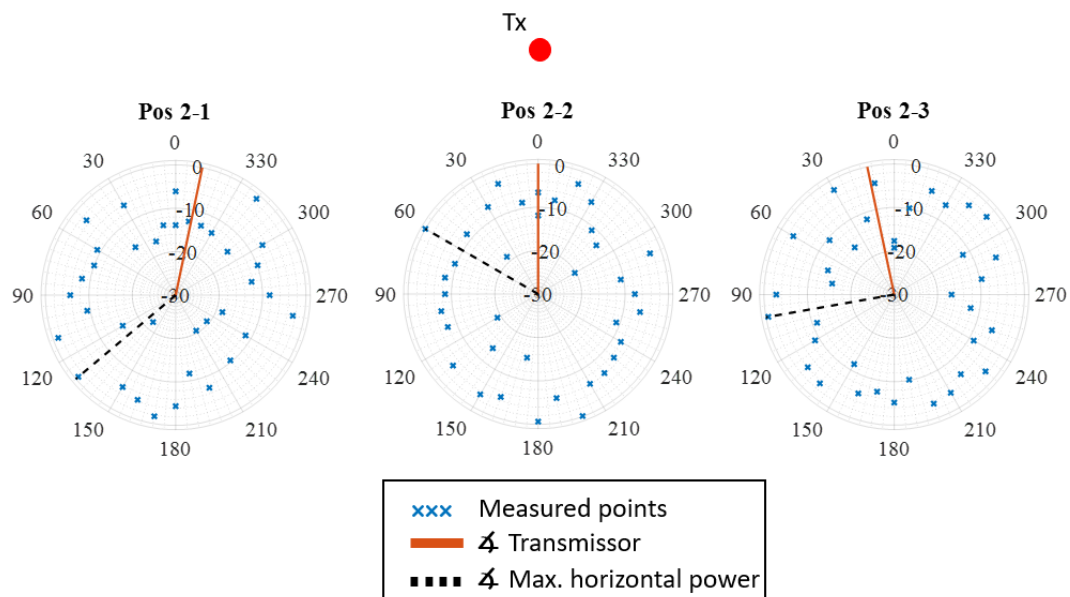


*Fig. 91 Indoor-indoor channel polar measurement between transmitter antenna and receiver antenna at three different positions. The receiver antenna is the designed reflector antenna with conformal*

*patches (Azimuthal rotation). Red line: physical angle between receiver and transmitter antenna. Black dotted line: direction of maximum power.*

## 4.2 Sub-6 GHz channel measurement

For the Sub-6 GHz band, the two conformal patches deployed in the reflector are used as receiving antennas, placed indoors (see Fig. 94 and 96). As transmitter a linear polarized Vivaldi antenna (see Fig. 95) is used.

In both cases a similar behavior is observed in Figs. 92 and 93 in the sense that in the positioning with LOS (pos 2-2) there is an alignment between the direction of maximum power and the angle at which the transmit antenna is placed. In both cases we can also identify other directions from which energy can be captured.

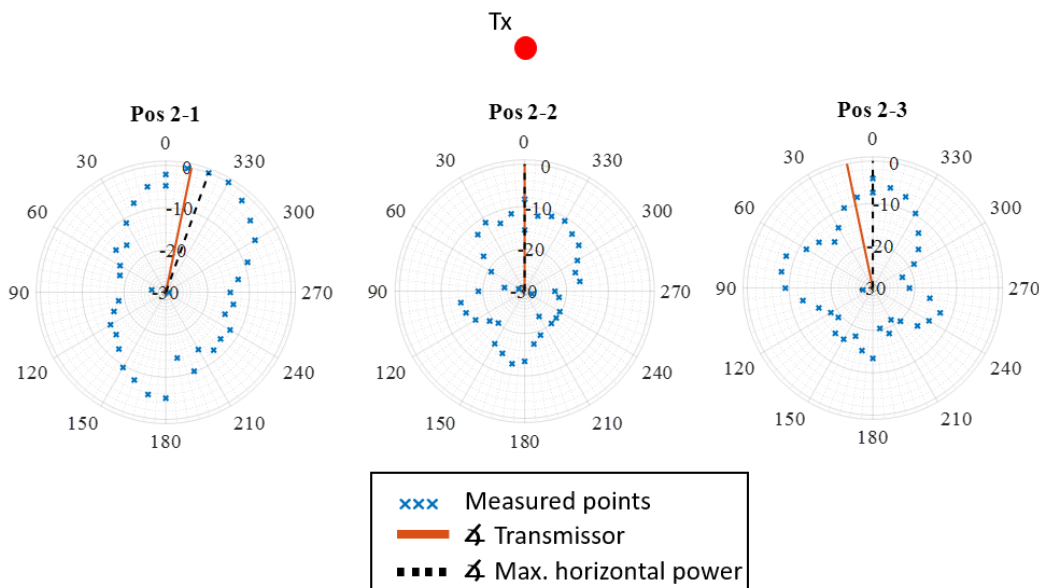


*Fig. 92 Indoor-indoor channel polar measurement between transmitter antenna and receiver antenna at three different positions. The receiver antenna is the bottom conformal patch to the reflector antenna and the transmitter is a linear polarized Vivaldi antenna (Azimuthal rotation). Red line: physical angle between receiver and transmitter antenna. Black dotted line: direction of maximum power.*

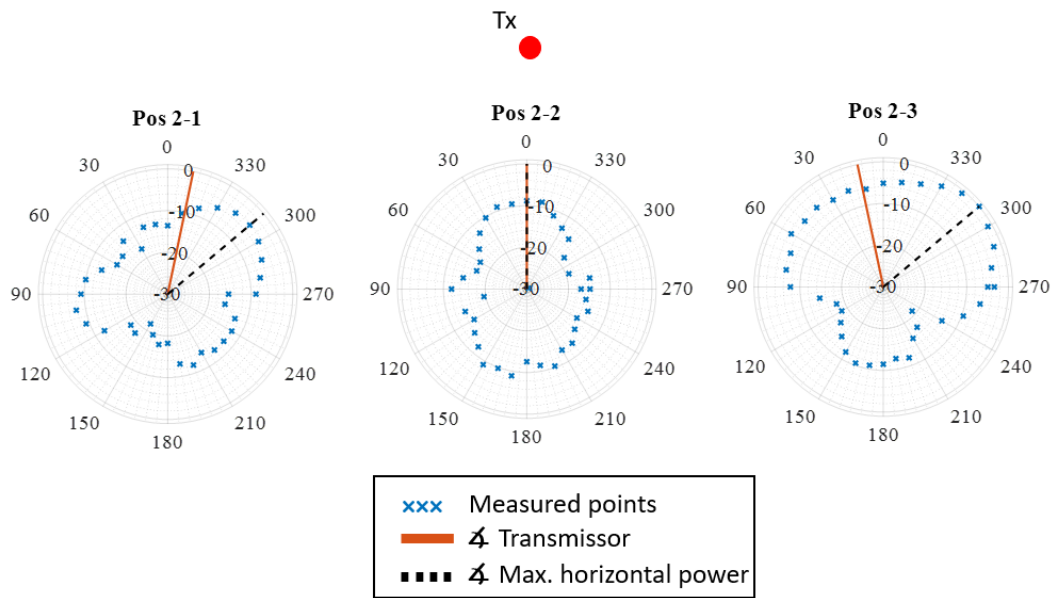


Fig. 93 Indoor-indoor channel polar measurement between transmitter antenna and receiver antenna at three different positions. The receiver antenna is the top conformal patch to the reflector antenna and the transmitter is a linear polarized Vivaldi antenna (Azimuthal rotation). Red line: physical angle between receiver and transmitter antenna. Black dotted line: direction of maximum power.

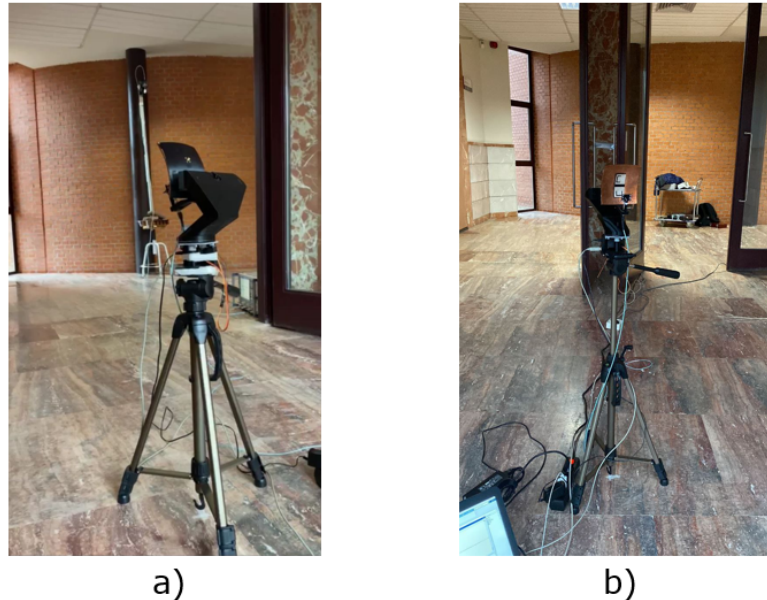


Fig. 94 Reflector antenna fed by phased array with conformal patches at reflectors surface. This antenna is used as channel measuring receiver antenna.



Fig. 95 Transmitter linear polarized Vivaldi antenna for sub-6 GHz measurements.



Fig. 96 Bottom "U" shape conformal patch antenna. Channel characterization measurement process.

## 5 Conclusions

This deliverable presents some final antenna designs to work on the dual band where two conformal patch antennas working in the sub-6 GHz band are deployed in the reflector of an antenna working in mm-wave. The proposed design and testing made validate the integration of both antennas enabling seamless dual-band service.

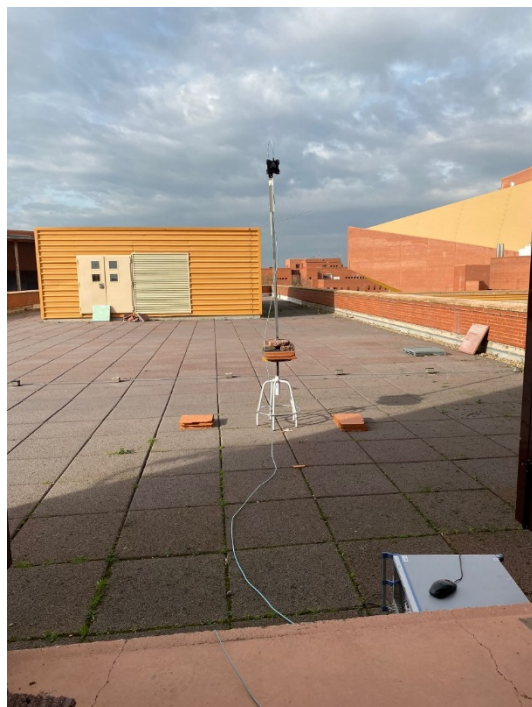
A detailed design procedure is provided in this document, that include the preliminary designs done by simulation the further implementation and the testing, validating the match between the designs and the real antenna performance.

Also the propagation scenario, identifying the most relevant directions for energy capture, is characterized, first for commercial horn antennas and latter for the designed antennas, showing that in real propagation scenarios, the dual-band antenna designed provided good performance.

## 6 Annex

Some additional pictures of the measurement system employed and the positioning of the receive antenna vs the transmit antenna is given.







## 7 References

- |                                                                                                                  |
|------------------------------------------------------------------------------------------------------------------|
| [1] Deliverable D7, "Implementation and Evaluation of Physical Antennas", 5GAFIANCE project, January 2021.       |
| [2] Deliverable D8, "Implementatios and Evaluation of Beam Control Algorithms", 5GAFIANCE project, January 2021. |